

# Distribution and characterization of failed (mega)blocks along salt ridges, southeast Brazil: Implications for vertical fluid flow on continental margins

Davide Gamboa,<sup>1</sup> Tiago Alves,<sup>1</sup> and Joe Cartwright<sup>1</sup>

Received 8 March 2011; revised 17 May 2011; accepted 1 June 2011; published 20 August 2011.

[1] Three-dimensional seismic data are used to assess the control of halokinetic structures on the distribution of blocks in a mass transport deposit in the Espírito Santo Basin, southeast Brazil. In contrast to what is commonly observed over growing salt structures, the thickness of the MTD-A1 is larger on top of a northwest trending salt ridge. Emphasis was given to the statistical analysis of 172 remnant and rafted blocks identified within Eocene mass transport deposits (MTD-A1). Three styles of block deformation are identified and scale relationships between the geometry of blocks and their relative position on the salt ridge are presented. Average block height reaches 130 m. Average block area reaches 0.43 km<sup>2</sup>, while 11.3% of the total area (A) investigated is covered by blocks (5% < A < 17%). On the basis of variations in block geometry (height, area, width/length ratio, orientation) and their relative distribution, we interpret that most failed strata have been remobilized by adjacent topography created during growth of the investigated salt ridge. We show that the origin of the blocks is linked to densely spaced sets of halokinetic-related faults that deformed the prefailure strata. The presence of underlying faults and blocks of remnant and rafted strata potentially induces sharp variations in the internal permeability of MTD-A1. Thus, the interpreted data shows that megablocks in MTDs can constitute viable fluid pathways on otherwise low-permeability units. This character can significantly decrease seal competence above and on the flanks of halokinetic structures.

**Citation:** Gamboa, D., T. Alves, and J. Cartwright (2011), Distribution and characterization of failed (mega)blocks along salt ridges, southeast Brazil: Implications for vertical fluid flow on continental margins, *J. Geophys. Res.*, 116, B08103, doi:10.1029/2011JB008357.

## 1. Introduction

[2] Halokinesis is triggered by loading gradients imposed by overburden rocks, with resulting deformation predominating during regional extensional events, or during shortening of preexisting salt structures [Hudec and Jackson, 2007; Jackson and Vendeville, 1994; Jackson et al., 1994; Vendeville, 2002]. In such a setting, the thickness and strength of overburden strata, sediment distribution patterns above salt, and the thickness of the original evaporitic units, together with regional and local tectonic stresses, can limit salt growth and induce geometric variability in growing salt structures [Davison et al., 1996; Dooley et al., 2009; Jackson and Hudec, 2005; Jackson et al., 1994; Schultz-Ela et al., 1993; Seni and Jackson, 1983]. In southeast Brazil this variability is expressed by a basinward transition from salt rollers, anticlines and pillows in proximal (extensional) regions, to salt walls, diapirs and stocks in

the midslope region. Salt canopies and sheets occur in distal compressional regions [Davison, 2007; Demercian et al., 1993; Fiduk et al., 2004; Mohriak, 1995].

[3] Deformation resulting from halokinesis is expressed by overburden faulting, regional folding and local subsidence, followed by gravitational collapse of flanking strata to salt structures [Davison et al., 2000a; Tripsanas et al., 2004]. Over growing salt diapirs, overburden strata is commonly either thinned or completely removed by erosional processes, which accumulate eroded strata in peripheral salt withdrawal basins [Giles and Lawton, 2002]. Mass transport deposits (or MTDs) resulting from these erosional processes are usually mud dominated and have low exploration potential [Lee et al., 2004; Moscardelli et al., 2006; Posamentier and Kolla, 2003], except when sand-rich strata is present [Armitage et al., 2009; Beaubouef and Abreu, 2010; Davison et al., 2000b; Dunlap et al., 2010; Moraes et al., 2007; Moscardelli and Wood, 2008; Piper et al., 1997; Shanmugam et al., 1996; Tripsanas et al., 2008]. Important factors controlling the seal competence of MTDs include the presence of a strong structural fabric (including faults) in their interior, and variations in the degree of remobilization experienced by failed strata [Frey-Martínez et al., 2006].

<sup>1</sup>3D Lab, School of Earth and Ocean Sciences, Cardiff University, Cardiff, UK.

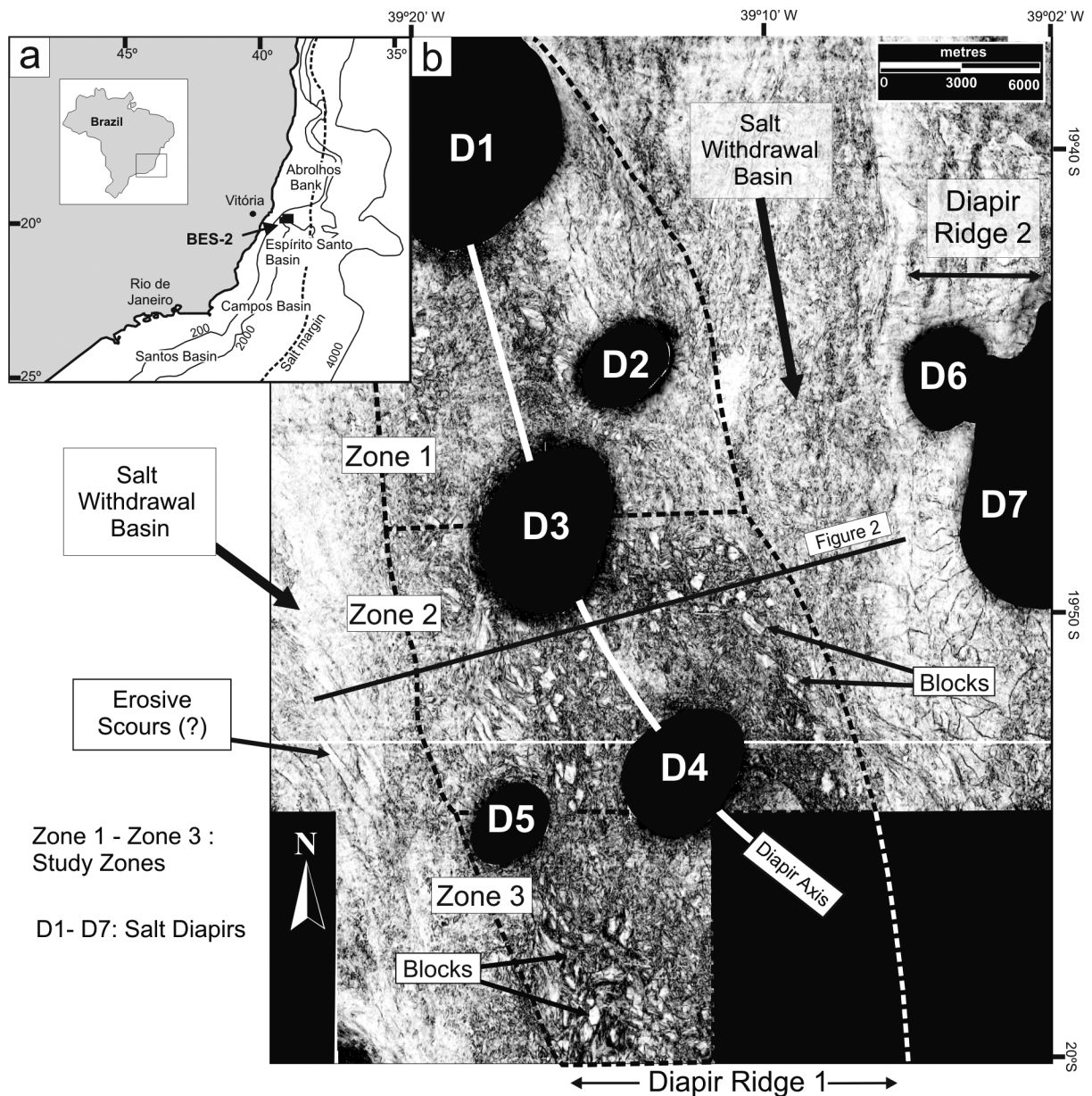


**Figure 1.** (a) Map of the southeast Brazilian margin showing the location of the Espírito Santo Basin. The location of the BES-2 3D seismic data set used in this study is represented by the black rectangle. (b) Coherence slice taken 20 ms TWTT above Horizon 1, intersecting the studied MTD. The studied MTD overlies a north-south oriented diapir ridge where five diapirs are present. This area was divided in three zones representative of upper, middle and lower slope, respectively. Numerous high coherence geometric remnant/rafted blocks (light colors) are observed within the limit of Diapir Ridge 1. Block clusters are observed in zone 3 and rims of zone 2. No blocks are observed either in the salt withdrawal basins or the region of Diapir Ridge 2.

Consequently, failed submarine strata are classified into submarine “slides,” “slumps” and “debris flows” based on their degree of internal cohesion [Masson *et al.*, 2006; Nemec, 1990]. Submarine slides are composed of coherent strata with minor internal deformation. The presence of slump deposits in a MTD implies larger travel distances and internal deformation than with slides. Debris flows are characterized by presenting highly disaggregated strata and no preservation

of internal strata within a cohesive matrix [Masson *et al.*, 2006]. Large blocks of remnant or rafted strata can be ubiquitous within the latter classes of submarine landslides, either close to the MTD source areas or transported to toe regions of submarine landslides through gravitational processes such as hydroplaning [Deptuck *et al.*, 2007; Dunlap *et al.*, 2010; Ilstad *et al.*, 2004; Lee *et al.*, 2004; Minisini *et al.*, 2007; Tripsanas *et al.*, 2008; Urgeles *et al.*, 2007].

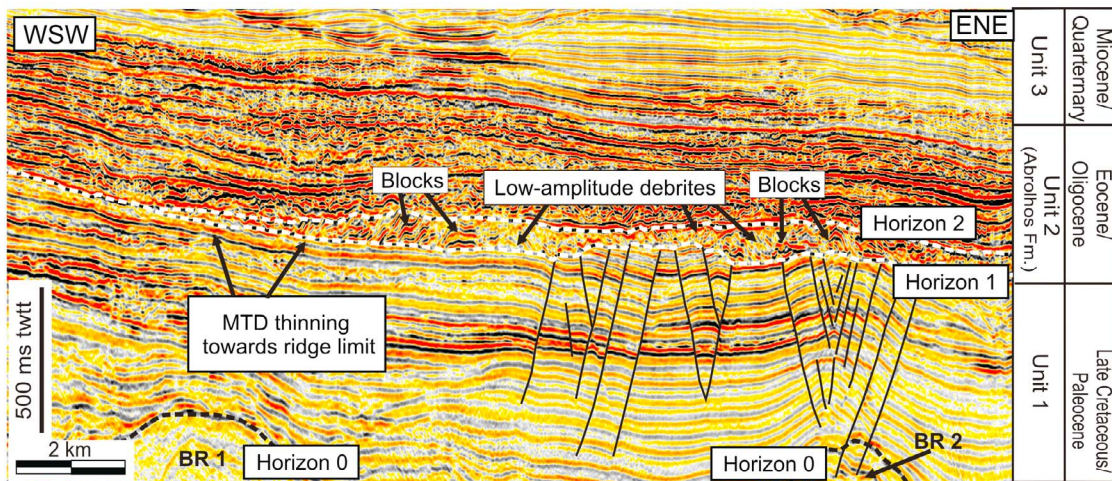


**Figure 2.** Seismic section representing the character of the identified seismostratigraphic units in northern Espírito Santo Basin. Unit 1 (Late Cretaceous–Palaeogene) is characterized by low-amplitude reflections. Crestal faults are present above buried salt ridges. Unit 2 is characterized by high amplitudes and chaotic character of the seismic reflections, contrasting with the remaining units 1 and 3. MTD-A1 is the lowermost deposit identified in unit 2, bounded by Horizon 1 and Horizon 2. This section also evidences thinning of the MTD toward the rims of the diapir ridge.

Individual blocks are named as “remnant” if left in situ, or “rafted” if substantially translated during slope failure. They have a wide range of sizes, from meters to hundreds of meters, but this tends to decrease with larger travel distances [Bull *et al.*, 2009; Canals *et al.*, 2004; Davison, 2004; Gee *et al.*, 2006].

[4] Rafted blocks have been comprehensively identified in the vicinities of salt structures, either derived from local failures [Davison *et al.*, 2000a; Tripsanas *et al.*, 2004] or distant (upslope) landslides [Dunlap *et al.*, 2010; Lee *et al.*, 2004]. However, no data has been yet presented on the effect of salt diapirs on slope stability, nor the impact of such remnant/rafted strata on fluid flow has been yet assessed for a key case study. In addition, no comprehensive reviews on the relative distribution of remnant/rafted blocks over salt structures have been attempted. In order to address these latter limitations, this work focuses on a MTD unit (MTD-A1) at the base of the Abrolhos Formation, an important Eocene–Oligocene stratigraphic unit in the Espírito Santo Basin, southeast Brazil [França *et al.*, 2007]. The Abrolhos Formation comprises vertically stacked MTDs intercalated with siliciclastic and volcanoclastic deposits [Fiduk *et al.*, 2004; Gamboa *et al.*, 2010; Mohriak, 2005] (Figures 1 and 2). Significantly, similar units occur in the Campos basin, where Eocene sand bodies intercalated with MTDs constitute viable reservoirs [Moraes *et al.*, 2007].

[5] In this paper, we characterize the internal fabric of MTD-A1 to assess the distribution of remnant/rafted blocks over salt structures which were actively growing at the start of the Eocene. We demonstrate how stratigraphic and/or structural permeable pathways for fluid flow can be present through otherwise poorly permeable MTDs. This will be primarily achieved by analyzing (1) the internal deformation and relative distribution of blocks above local diapir ridges, (2) the effect of underlying fault families on the generation and distribution of blocks above diapir ridges, and (3) the

relative importance of block and fault distribution to vertical fluid flow through salt structures.

[6] The paper starts by describing the geological setting of the Espírito Santo Basin, the data and methods used and the seismic stratigraphy of the studied survey. It will then describe the relevant features of the basal MTD using key seismic profiles and seismic attribute maps, and a quantitative analysis of block properties. In the end, we discuss the occurrence of blocks and their relation to fault families in the study area, the significance of the investigated MTD-A1 as marker of halokinesis, and how the distribution of the blocks in the MTDs above the diapir ridges can influence the vertical permeability of the MTD units. Major faults similar to those identified in the study area constitute migration paths for hydrocarbons in the Campos basin, linking the Cretaceous source rocks to Cenozoic reservoirs in the basin [Guardado *et al.*, 1989, 2000; Mello *et al.*, 1994; Mohriak *et al.*, 1990]. A similar mechanism to that identified in the Campos Basin has been suggested for the Espírito Santo Basin [Biassussi *et al.*, 1998].

[7] In this work, the terms “blocks” or “megablocks” [Spence and Tucker, 1997] are used to describe large blocks of strata, some reaching hundreds of meters in height and width. Remnant and rafted blocks of strata are shown as partly geometric features with high reflection strength (Figure 3). In the study area, remnant blocks are bounded by faults propagating from underlying strata and do not show any significant disruption of strata at their base (Figure 3). In contrast, debris and other mass wasting strata are seen as low-magnitude features within MTD-A1 (Figures 3a and 3b). They comprise individual blocks embedded in low-amplitude to chaotic strata and present significant disruption of basal strata at, or adjacent to, the glide plane (Figure 3). The base of the study interval is densely faulted, with developed normal faults occurring predominantly on the crest of buried salt diapirs and ridges. Their upper tips are commonly truncated by a mid-Eocene erosive surface,

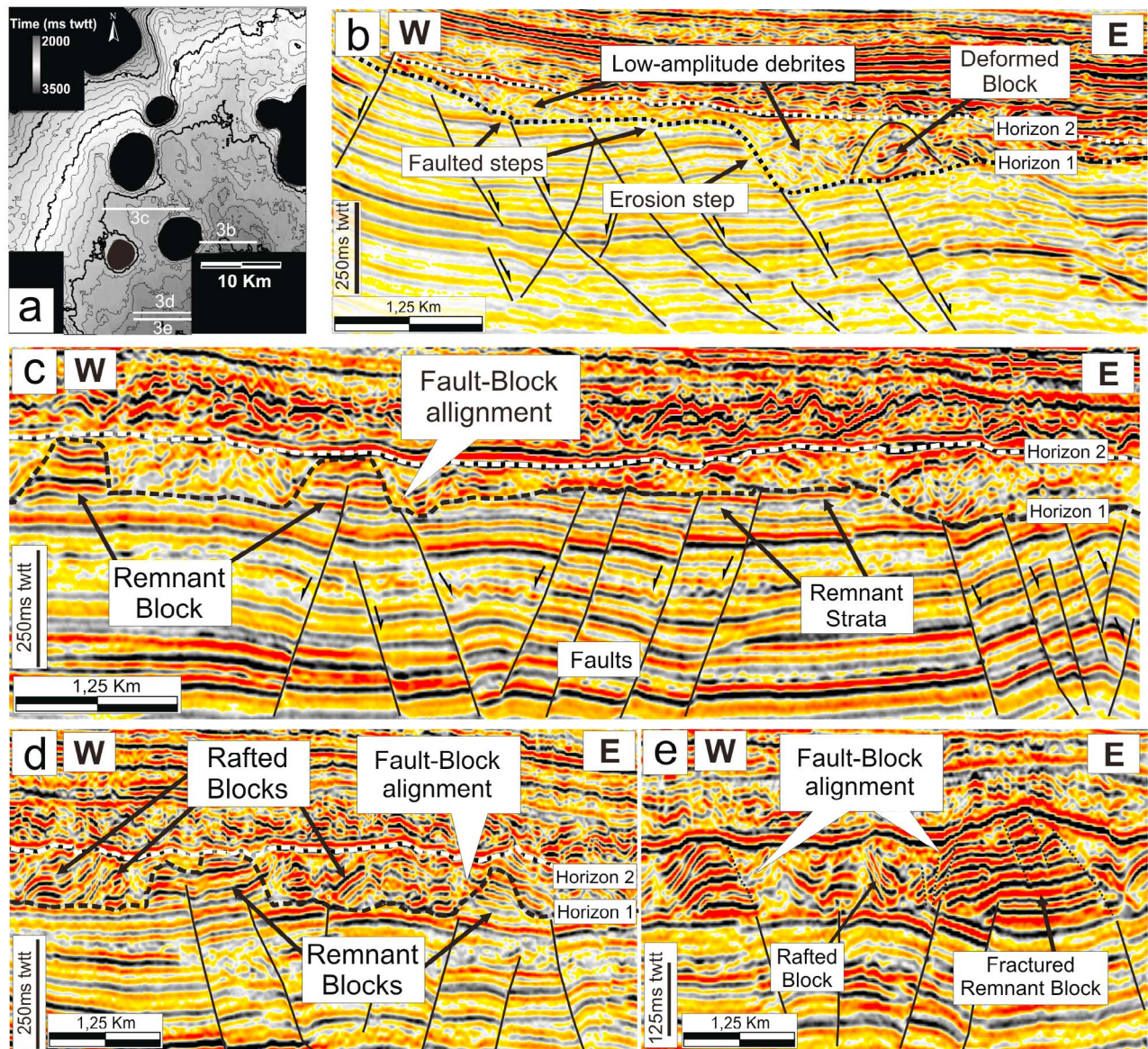


**Figure 3.** Seismic sections depicting the relation between faults and blocks. (a) Map showing the location of seismic sections. (b) Stepped profile of Horizon 1, showing evidence of the influence of preexisting faults on the mass failure. The small steps in the horizon irregular profile are due to fault activity, whereas high steps are due to remobilization of failed strata. The latter is confirmed by the height of the deformed block, similar to the height of the erosional step. (c) Section of MTD-A1 depicting the relation between faulting and remnant strata/blocks. The remnant features show evident vertical continuity with the underlying unit, limited by the erosional surface. Notice the thicker accumulations on the eastern sector underlain by faults. (d and e) More detail of the link between blocks and prefailure faults. The blocks commonly show their limits aligned with the faults, especially less deformed ones. Fractures are commonly identified within the bigger blocks. Rafted blocks show titled or folded internal reflections, implying lateral movement. Fault block alignments are less evident in this type.

with some of the faults propagating into remnant/rafted strata with MTD-A1 (Figures 3c and 3d).

## 2. Data and Methods

[8] The 3D seismic survey used in this study covers an area of approximately 1600 km<sup>2</sup> in the Espírito Santo Basin,

at water depths that range from 100 to 1800 m (Figure 1a). During data acquisition a dual air gun array and six, 5700 m long streamers were used. Signal was sampled at 2 ms and zero-phased migrated with a 12.5 m grid line spacing (inline and crossline).

[9] We complemented the information provided by key seismic profiles with computed seismic attributes, namely

root-mean-square (RMS) amplitude maps and coherence slices in order to visualize the correct geometry of remnant/rafted blocks. The RMS amplitude attribute shows the average squared amplitude values from individual amplitude samples within a defined interval [Brown, 2004]. Coherence attributes convert a seismic volume of continuity (normal reflections) into a volume of discontinuity, highlighting faults and stratigraphic limits [Brown, 2004]. All coherence slices were computed above a volume flattened at Horizon 1, the base of MTD-A1. This horizon was used in order to assess the presence of blocks and other MTD features at equal time intervals above the basal surface. In addition, isochron maps were computed in order to evaluate the two-way (twtt) thickness variations between defined intervals. Measurements of block height were obtained by direct measurement on vertical seismic profiles. Time conversions in the studied interval were made using an estimated seismic velocity of 3100 m/s twtt based on the velocity profiles measured for the base of Eocene strata at DSDP site 516 [Barker et al., 1983]. On the basis of this velocity and using a computed dominant frequency of 40 Hz, we estimated a vertical resolution of 19 m at the studied stratigraphic interval. The distances of block length and width, as well as block area were directly measured on a MTD base map. On the basis of the horizontal resolution of the seismic data, an error of 12.5 m and 0.000156 km<sup>2</sup> is estimated for measured distances and areas, respectively.

[10] To simplify our analysis, the studied portion of the MTD was subdivided into three subregions, zone 1, zone 2 and zone 3, based on their relative position on the studied slope and on relative block density along the main salt ridge (Figure 1b). Linear regressions, when computed, were tested using residuals analyses [Seber and Lee, 2003]. Residual analysis is important as a method of testing how well a model captures the behavior of the data, by plotting a series of residuals plots for the acquired data values [Jensen et al., 2007]. When used, residuals plots showed the distribution of data to be correctly represented by linear regressions.

### 3. Geological Setting

#### 3.1. Depositional Units

[11] The Espírito Santo Basin is located offshore southeast Brazil and is bounded by the Abrolhos Plateau to the north and the Campos Basin to the south (Figure 1a). The Espírito Santo Basin resulted from the breakup of West Gondwana in the Mesozoic, an event that resulted in formation of Late Jurassic to Cretaceous rift basins in the South Atlantic [Davison, 1999; Fiduk et al., 2004; Mohriak et al., 2008]. The postrift evolution of the study area includes an Aptian–early Albian transitional stage. During this stage, thick evaporitic sequences were deposited. The Late Cretaceous drift stage is characterized by an early transgressive megasequence associated with the deposition of an Albian shallow water carbonate platform, followed by late Albian to Palaeogene pelitic shales [Demercian et al., 1993; Mohriak et al., 2008; Ojeda, 1982]. These shales are buried under late drift Eocene–Holocene marine regressive siliciclastic sequences related to slope progradation [Fiduk et al., 2004; Mohriak, 2003]. Separating both megasequences there is a mid-Eocene sequence boundary present along the entire southeast Brazilian margin [Moraes et al., 2007], which

forms the base of the MTD succession investigated in this work (Figure 2).

#### 3.2. Cenozoic Tectonism

[12] The Cenozoic evolution of the proximal Espírito Santo Basin is predominantly controlled by thin-skinned extension above Aptian evaporites [Fiduk et al., 2004]. In the midslope regions, halokinesis formed northwest trending sediment fairways. Thus, extensional salt rollers occur in proximal areas, well-developed diapirs are observed in midslope locations, and overhangs or allochthonous canopies in distal slope regions [Davison, 2007; Demercian et al., 1993; Fiduk et al., 2004; Mohriak et al., 1995]. Salt structures in the Espírito Santo Basin developed significantly through the Late Cretaceous and Cenozoic, together with evident deformation of the modern seafloor [Fiduk et al., 2004]. Important to the analysis undertaken in this paper is that distinct faulting stages have been identified in the Espírito Santo Basin in association with the episodic growth of salt structures [Alves et al., 2009; Baudon and Cartwright, 2008]:

[13] 1. A first episode of faulting resulted in the formation of closely spaced synclinal and crestal faults that propagate through the Late Cretaceous and Eocene strata. These faults are mostly truncated by the mid-Eocene unconformity, which also marks the base of MTD-A1 (Figure 2).

[14] 2. Faulting of Late Eocene to Holocene strata is less expressive, occurring predominantly by reactivation of older faults over collapsed salt anticlines. These reactivated faults have poor or no expression on the modern seafloor [Alves et al., 2009; Baudon and Cartwright, 2008].

[15] Together with widespread halokinesis, Eocene uplift of the hinterland mountain ranges and volcanic activity on Abrolhos Plateau region also played a significant role in the evolution of the Espírito Santo Basin. Tectonic tilting of the margin, and the resulting increase in sediment input onto the continental slope, resulted in a peak in halokinesis during the Late Cenozoic [Fiduk et al., 2004; Lima, 2003].

#### 4. Seismic Stratigraphy

[16] The study area comprises three main seismostratigraphic units, depicted in Figure 2. Unit 1 is Upper Cretaceous to Paleocene in age [Baudon and Cartwright, 2008], with its top marked by the mid-Eocene unconformity [Fiduk et al., 2004; Gamboa et al., 2010]. Unit 1 shows moderate amplitude, continuous reflections. The lowermost packages show growth strata on the rims of the diapirs. At the top of the unit, reflections tend to be sub-parallel, with minor thickness changes. This stratigraphic interval is densely faulted, with developed normal faults occurring predominantly on the crest of buried salt diapirs and ridges. Their upper tips are commonly truncated by the mid-Eocene erosive surface at the base of MTD-A1 (Figures 2 and 3).

[17] The base of unit 2 coincides with a regional mid-Eocene erosional unconformity [Gamboa et al., 2010]. The top is inferred to be of Miocene age, and is marked by contrasting high-amplitude in unit 2 and low-amplitude reflections in the overlying unit 3. In unit 2, the predominance of high-amplitude reflections is related to its content in volcanoclastic sediment. Therefore, its age is interpreted

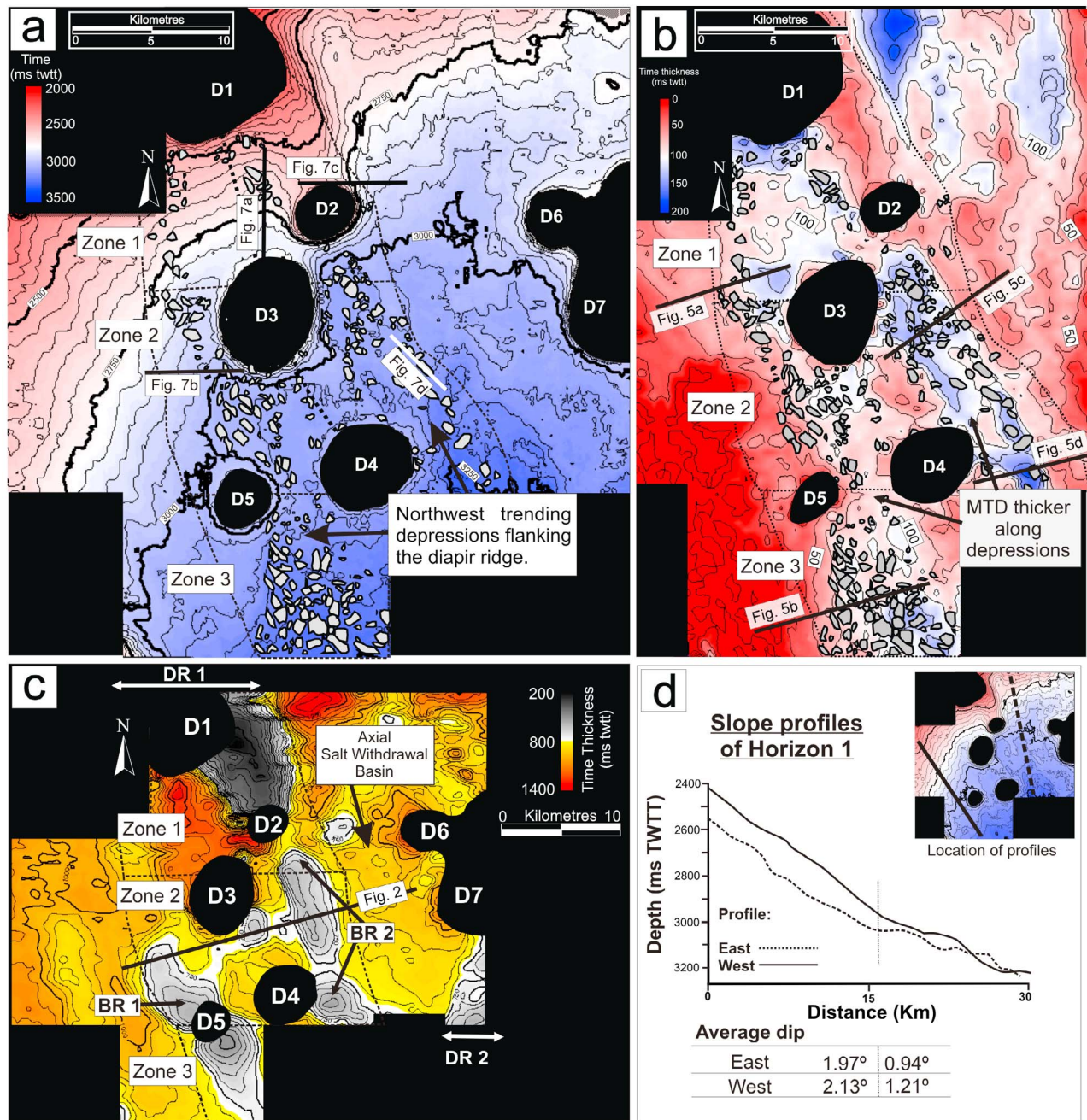


**Figure 4.** (a) Time map of Horizon 1, representing the base of MTD-A1. The gray shapes represent the blocks identified in MTD-A1, occurring along the northwest trending depressions flanking the ridge. Notice the higher abundance of blocks below 3000 ms twtt. (b) Isochron map of MTD-A1. The thickest MTD accumulations are present along the depressions of Horizon 1 pointed in Figure 4a, reaching close to 200 ms twtt, also coincident with the presence of the blocks. Other higher thickness deposits of the MTD are observed upslope of diapir D2, where no blocks occur. (c) Thickness map between Horizon 1 and Horizon 0, showing evidence of the Late Cretaceous deformation in the study area. Lower thickness (<750 ms) highlight the presence of buried salt ridges (BR1 and BR2) related with the smaller diapirs D5 and D2. (d) Slope profiles of Horizon 1 along the west and east flanks of the diapir ridge. The slope dip decrease coincides with slope regions where blocks occur.

to span the Eocene/Oligocene [Fiduk et al., 2004; Mohriak, 2003, 2005; Sobreira and França, 2005]. Chaotic and mottled reflections predominate in the unit, reflecting a significant abundance in mass wasting deposits. High-

amplitude subparallel reflections at places alternate with chaotic packages (Figure 2).

[18] The uppermost unit 3 is characterized by continuous parallel to subparallel strata, with low to moderate seismic

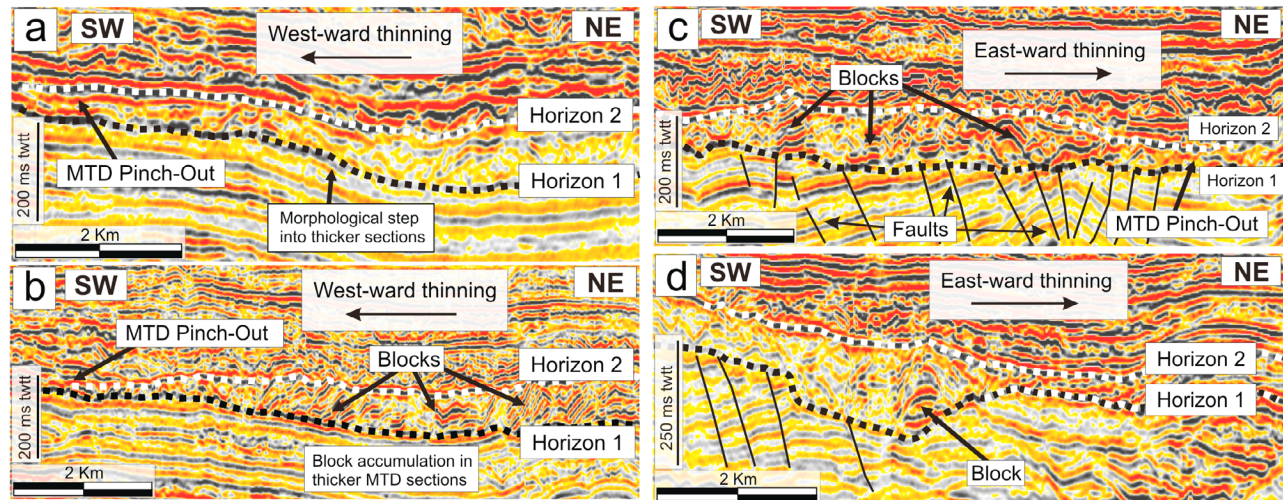


**Figure 5.** Seismic profiles illustrating the thinning of MTD-A1 toward the western and eastern limits. (a and b) Evidence of the morphological step of Horizon 1 which limits the regions of higher thickness of the MTD. (b–d) Blocks in the morphological depressions where thicker accumulations occur. The thickness of MTD-A1 is commonly defined by the block height, and these are absent in the thinner regions.

amplitude toward its base. Multiple channel systems are observed toward its top (Figure 2).

## 5. Character of the Basal MTD-A1

[19] This paper focuses on the lowermost MTD-A1 of unit 2, which overlies the mid-Eocene erosional unconformity. MTD-A1 is bounded by Horizon 1 and Horizon 2 (Figures 2 and 3), and covers about 955 km<sup>2</sup> within the area covered by the survey (Figure 4). Its base, Horizon 1, consists in an irregular, hummocky horizon marking the basal glide plane. The time structural map of this surface (Figure 4a) illustrates two distinct morphological trends. Steeper slope angles are observed in upper slope regions (average 2°) decreasing to 1° below 2900 ms. This decrease in slope is related to the presence of two northwest trending depressions along the flanks of the salt diapir ridge where the majority of the blocks are concentrated (Figure 4a). On seismic profiles, the transition to these depressed areas is marked by a morphological step, which also delimits the rims of MTD-A1 (Figure 5).

[20] A computed isochron map shows that MTD-A1 reaches its largest thickness in the salt region along the northwest trending depressions (Figure 4b). The thickness values observed here are over 75 ms twtt and reach a maximum of 175 ms twtt. Other thick deposits in this MTD are seen on the upper slope regions northeast of diapir D2, and outside of the main study area where thickness values reach up to 200 ms TWTT and no blocks are observed. Of particular relevance is that the thicker parts of MTD-A1 occur together with the regions of higher block density, over the developed salt structures (Figures 3 and 4).

[21] Figure 4c illustrates an isochron map between a Late Cretaceous horizon (Horizon 0) and Horizon 1, showing evidence of early relief created by halokinesis. The map shows two minor northwest trending buried salt ridges (named BR1 and BR2) and the diapirs within the studied main diapir ridge (DR1). Diapirs D2 and D5 are located

along the buried ridges BR2 and BR1, respectively. On the vicinities of the main diapir ridge focused on this study there are two axial salt withdrawal basins. On the easternmost locations of the survey there is a secondary north trending diapir ridge (DR2) from where diapirs D6 and D7 emerge. The comparison of the latter map with the isochron map in Figure 4b shows that the thicker accumulations of MTD-A1 overlie DR1.

### 5.1. Internal Character of the MTD

[22] The internal character of the studied MTD is varied, with high-amplitude sections grading or contacting with low to transparent amplitudes (Figure 3). The identification of internal features composing MTD-A1 allows the assessment of its flow and, for the purpose of this paper, to identify elements with the potential to allow fluid percolation through the failed strata. The features interpreted on seismic data will be described in detail in the following sections.

#### 5.1.1. Remnant and Rafted Blocks

[23] Blocks of strata within MTD-A1 were identified by the presence of moderate- to high-amplitude reflections within the low-amplitude, chaotic seismic reflections that comprise adjacent debrites (Figures 2 and 3). The recognition of geometric features on coherence slices (Figure 1b) and amplitude maps (Figure 6) allowed a more detailed analysis of the blocks' morphology. Remnant blocks are identified as being in situ, representing elements from the prefailure strata that were not removed by erosion. Such blocks show vertical stratigraphic continuity with underlying non-MTD strata, with absence of any gliding surface, similar to the features described by *Moscardelli et al.* [2006] and *Alves* [2010]. The identification of remnant features also had on account the relation between the block edges and any underlying faults. In contrast, rafted blocks are considered to have been transported downslope and commonly rest on top of the gliding surface (Horizon 1), although some are seen "floating" within the disaggregated chaotic matrix of the MTD.

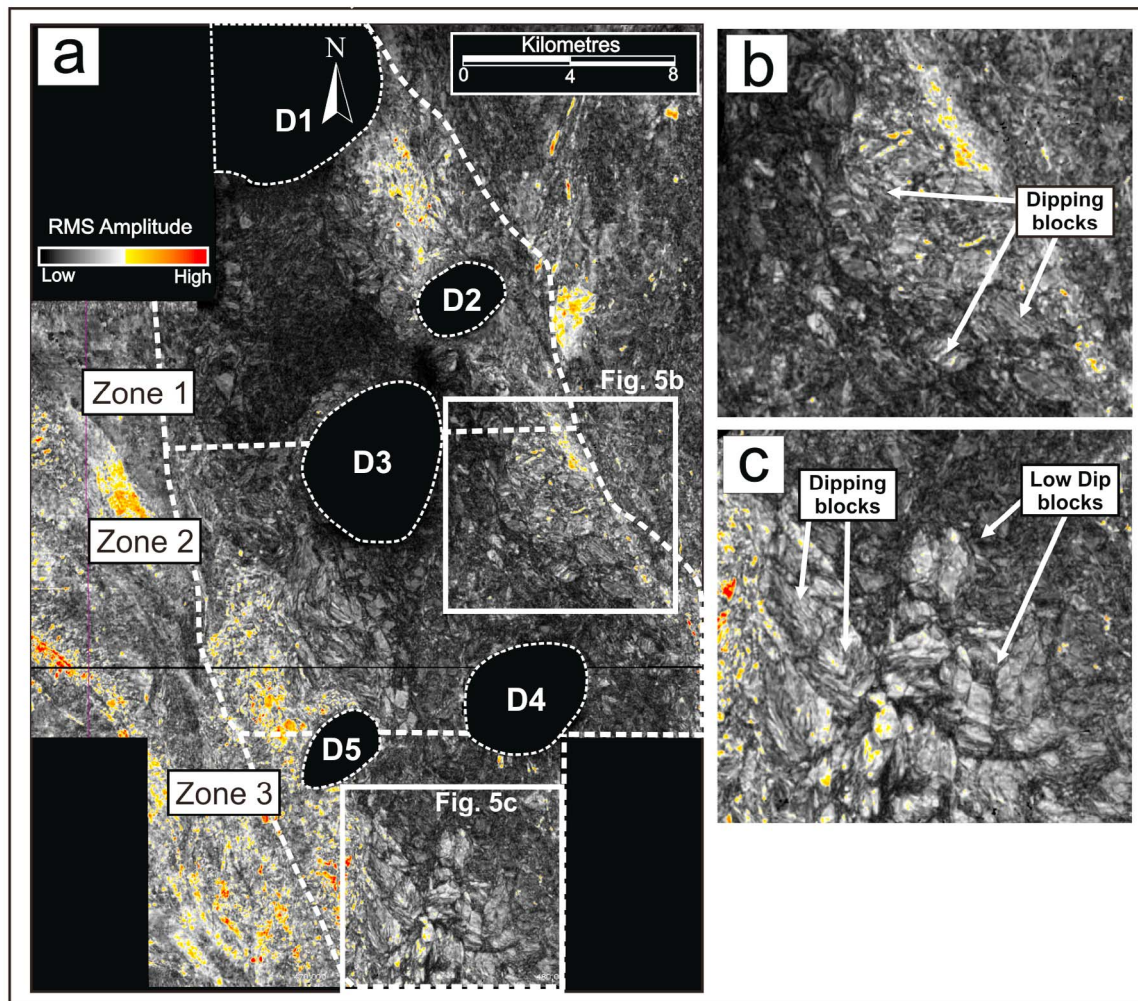


**Figure 6.** (a) Root-mean-square (RMS) amplitude map of a time window within MTD-A1 between 20 and 40 ms twtt above Horizon 1. Higher amplitudes are observed closer to the rims of the MTD, whereas the axial area of the ridge shows lower amplitudes. The blocks are evidenced by higher RMS amplitude values. (b) Detail of blocks with dipping internal strata evidenced by the alternations of pattern in RMS amplitude. (c) Detail of blocks with variable internal dip. The RMS amplitude maps provides an indicator of block deformation as tilted blocks show the banded internal aspect, whereas nontilted ones have relatively uniform amplitude patterns.

[24] The geometry of remnant and rafted blocks was assessed by combining coherence data and RMS amplitude maps (Figures 1b and 6). Figure 1b represents a coherence slice taken 20 ms above horizon H1. The chaotic sections of the MTD are represented by dark, mottled patterns. The blocks are clearly distinguished within these mottled areas as coherent subgeometric features with sharp edges. Individual blocks are commonly in contact with each other where higher densities are observed, as in zone 3. The majority of blocks are confined along the northwest trending depressions observed on the diapir ridge, being practically absent away from it (Figures 1b and 6).

[25] Rms amplitude maps show similar results to the coherence slices (Figure 6a). The map in Figure 6a represents an interval 20 to 40 ms twtt above Horizon 1. The geometry of the remnant and rafted blocks is evidenced by moderate- to high-amplitude features with geometric to subgeometric shape, as previously mentioned from the coherence data

(Figure 1b). However, in contrast to coherence data, the RMS amplitude map in Figure 6 shows that the blocks are not uniform. A significant amount of the blocks in zone 3 are distinguished by their high-amplitude values. Lower amplitude blocks also prevail in zones 1 and 2, where they are harder to be distinguished from adjacent failed strata. RMS amplitude data can, however, highlight the presence of parallel bands inside imaged blocks, which often relate to the presence of dipping strata in the blocks (Figure 6b). Such features indicate block deformation and rotation, namely stratal dip, which also provides indications to assess the transport direction of the MTD. These features are characteristic of rafted blocks.

[26] Unless otherwise stated, the term “blocks” used in this study regards both types indistinctively of being remnant or rafted. This is used as a simplification when the block-related processes or properties are considered to be identical.

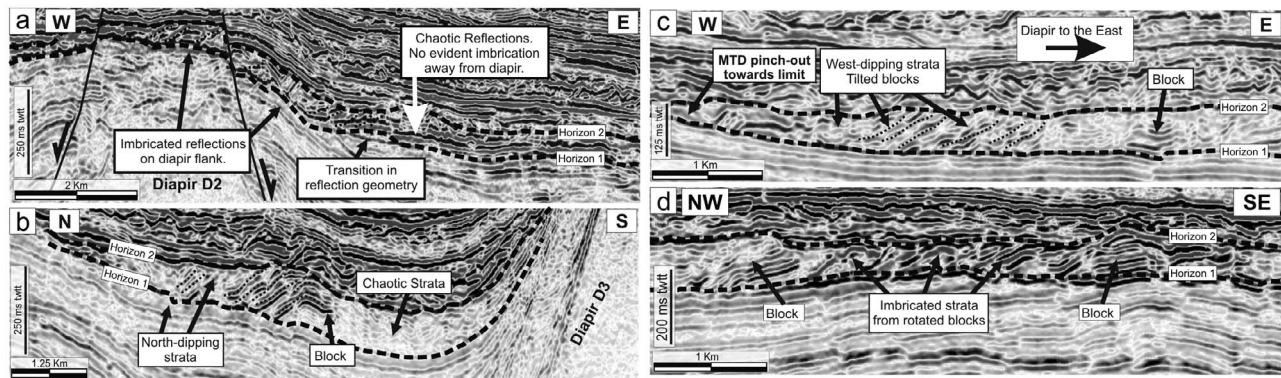


**Figure 7.** Seismic sections depicting internal imbrications in the MTD, used as kinematic indicators of the MTD transport direction. (a) Seismic section north of diapir D2, showing imbrications dipping toward the diapir, indicating eastward flow toward the salt withdrawal basin. The evident imbrications on the top and flanks of the diapir suggest a flow collision with the chaotic masses in the salt withdrawal basin. (b) Section on the northern flank of diapir D3. Imbricated strata indicates southward movement of this MTD component, buttressing against the diapir. (c) Section on the rim of MTD-A1, where imbricated blocks evidence eastward flow of a peripheral component toward the diapir ridge. (d) Example of imbricated strata on the eastern regions of the salt ridge. This section evidences differential MTD internal flow. Rotated blocks have their movement hindered by larger, less remobilized blocks.

### 5.1.2. Internal Imbrication

[27] Within MTD-A1 the stratal imbrications are evidenced by high-amplitude reflections dipping away and toward the observed diapirs (Figure 7). The best examples are observed on the eastern flank of the main diapir ridge, on the northern flank of diapir D2 (zone 1) (Figure 7a). Strata imbrication is observed along the flank of the diapir D2. At the transition point toward the axial salt withdrawal basin the MTD seismic character changes into the chaotic reflections with no obvious organization. These also correlate with thinner sections of the MTD, which gradually thickens as dip decreases. The section described is not related to any blocks in the coherence and RMS amplitude maps, therefore it is interpreted as being related to compression resulting from movement perpendicular to salt ridge SR2.

[28] We interpret the majority of imbricated features identified in seismic profiles as rotated rafted blocks (Figure 7b). Although on key seismic profiles their character is similar to compressional features, the coherence and RMS amplitude maps show a limited coverage for the higher-amplitude dipping strata, being surrounded by low-amplitude chaotic reflections. The blocks often dip away from the diapirs, as in Figures 7b and 7c, being bounded by normal and reverse faults (Figure 3 and section 5.1.3). Despite the distinct orientation in Figures 7b and 7c, they suggest to represent collapsed blocks flowing toward the central areas of the salt ridge. Other cases also show that the rotated/imbricated blocks also occur in close association with less deformed blocks (Figure 7d). This is common in the major block clusters within MTD-A1, meaning that in these sections the blocks' movement should have been more complex.

### 5.1.3. Fault Distribution and Relation to Failed Blocks

[29] The majority of faults in unit 1 are truncated by the mid-Eocene unconformity that limits the unit, with some propagation above this same surface. Propagating faults are in the study area related with halokinetic deformation [Alves

*et al.*, 2009], forming polygonal-shaped fault sets in unit 1 (Figures 8a and 8b). The relation between faulting and the presence of blocks is particularly evident on the eastern section of zone 2 and the majority of zone 3, also coincident with the presence of underlying salt ridges (Figure 8c). A quantitative comparison of the area of the blocks and the fault spacing below Horizon 1 revealed that, on average, the area of fault spacing in zone 2 is 0.28 km<sup>2</sup> and block area is 0.31 km<sup>2</sup>. As for zone 3, the average areas of fault spacing and blocks are 0.38 and 0.36 km<sup>2</sup>, respectively. The proximity of faults and blocks, in particular remnant ones (Figure 3), plus their similar trends suggest a genetic link between both features. Key seismic profiles also evidence the relation between faulting and the features present in MTD-A1 (Figure 3). East of diapir D4, preexisting faults are suggested to limit regions later deformed and evacuated by the mass wasting event. Although Horizon 1 probably had a stepped profile due to fault offsetting, the most prominent step and consequently a section of higher MTD thickness is well delimited by one of the Palaeogene faults. The presence of a deformed rafted block with approximately the same height as the morphological step, plus the cut of several reflections in unit 1 support the hypothesis that the irregularity of the gliding surface is equally due to tectonic and erosional processes (Figure 3b).

[30] The most evident link between blocks and preexisting faults is seen above buried salt structures in zone 3 and zone 2 (Figures 3c and 3d, respectively). The limit of remnant blocks is often aligned with the direction of underlying faults, especially in cases where blocks with subhorizontal internal strata are observed, or where their downslope movement was hindered (Figures 2 and 3). This character is more common in larger blocks or in locations where fractured remnant blocks with evident internal faults, but not completely broken, occur (Figure 3e). In general, the regions with higher fault density are the ones with higher number, and larger sizes, of blocks.

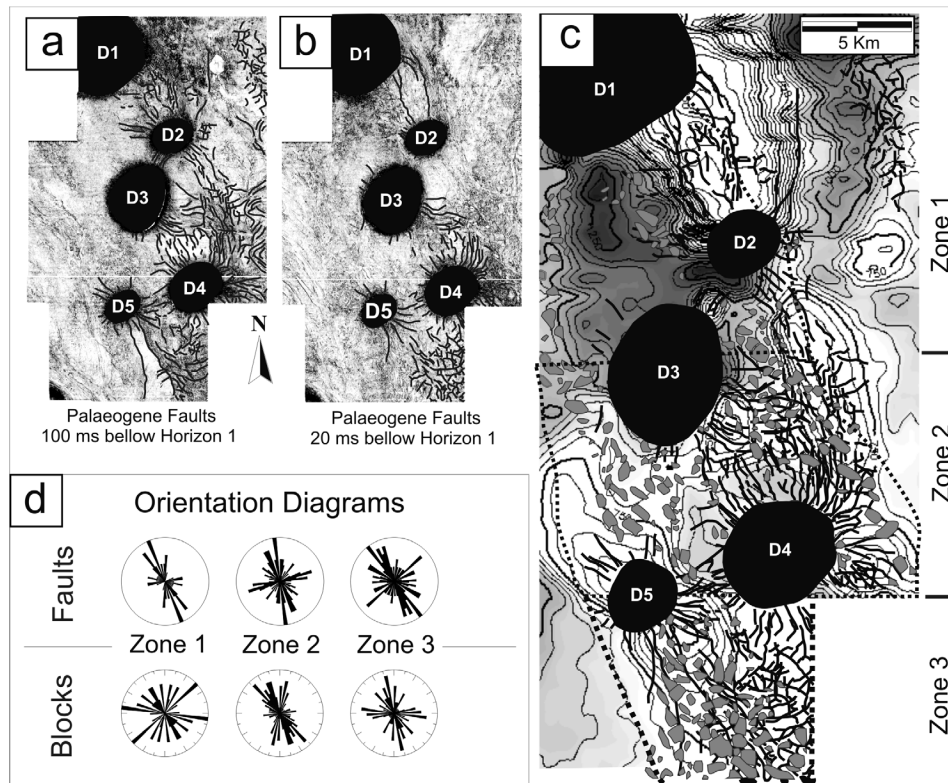


**Figure 8.** Fault block relation. (a) Coherence map of a slice taken 100 ms twtt below Horizon 1, showing the faults in unit 1. (b) Coherence map of a slice taken 20 ms twtt below Horizon 1. These maps show important faulting of unit 1 along the southern and eastern regions of the diapiric ridge. (c) Map showing evidence of the buried salt ridges and the modern diapirs with the overlay of the faults in unit 1 and the blocks in MTD-A1. The ridges, faults and blocks show a close relation in zone 3 and the eastern region of zone 2. Note how the more fractured areas correspond to the ones where block frequency is higher. (d) Rose diagrams with the fault and block orientation along the diapir ridge. Both features show preferential northwest trending directions.

## 5.2. Peridiapiric Block Distribution

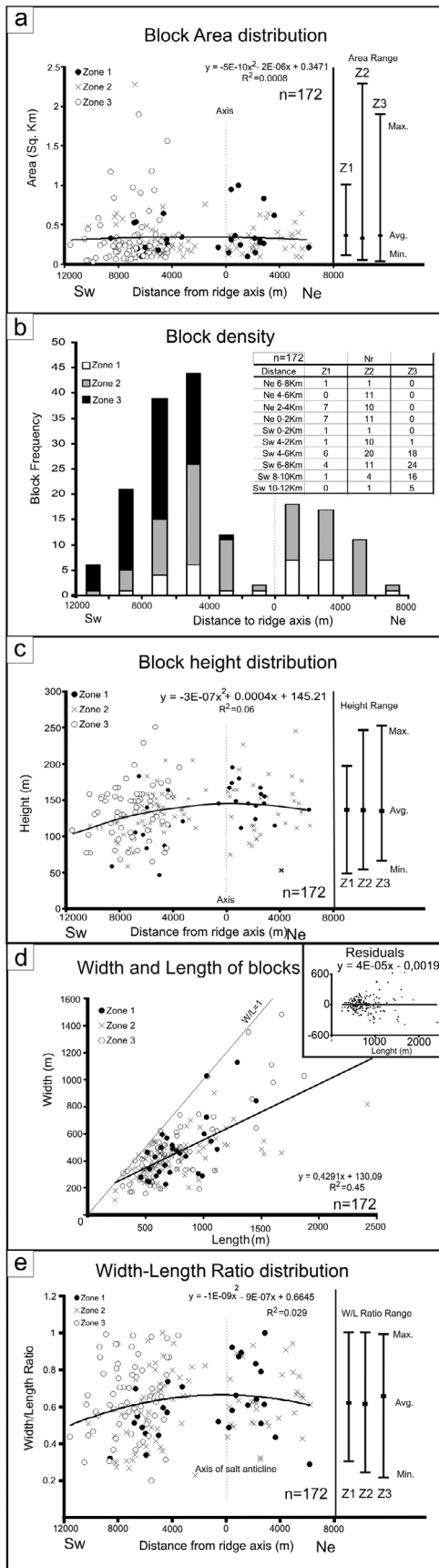
[31] This section shows the results of a quantified analysis of block characteristics and distribution. For this we considered the three zones previously mentioned in order to identify any significant statistical variations across the investigated diapir ridge. A total of 172 blocks were analyzed. We measured their height, length, width, area, orientation (long axis) as well as distance from the established diapir ridge axis. The results are illustrated as graphs in Figure 9. The data is represented in relation of: 1) the block distance to the diapir ridge axis and 2) the position relative to the reference, i.e., East or West of the axis. The range bars in 9a, 9b and 9e represent the minimum, maximum and average value of the represented parameters for each zone. The block density plot (Figure 9b) illustrates the number of blocks per zone identified at a given distance from the diapir ridge axis. The quantitative analysis of variations in block properties not only allows an evaluation of the origin and evolution of the MTD, as it will also characterize the possible fluid conduits through the failed strata. It should be pointed out that, due to survey limitations, in zone 3 we can only consider the blocks west of the diapir axis. From the total 28 were located on zone 1, 80 on zone 2 and 64 on zone 3.

### 5.2.1. Block Surface Area

[32] The total area (A) covered by the blocks is in average 11.3% over the diapir ridge. However, these values vary within the three investigated zones such as  $4.96\% < A < 17.32\%$ . The relative proportion of blocks in each subzone shows that these cover 4.96% (10.11 km<sup>2</sup>) of zone 1, 11.60% of the area (25.17 km<sup>2</sup>) in zone 2, and 17.32% (22.76 km<sup>2</sup>) of zone 3. The larger block is located in zone 2 (2.3 km<sup>2</sup>) and the majority of the blocks with surface area higher than 1 km<sup>2</sup> are located in zone 3 (Figure 9a), but 85% of the studied blocks have areas below 0.5 km<sup>2</sup>. Average block size is 0.4 km<sup>2</sup>, similar in the three zones. The similar average values for the area in the three zones suggest a similar evolution for the blocks along the slope, as they should be expected to show significant variations toward downslope regions. In addition, this analysis is also important to estimate the areal extent of hypothetical fluid conduits.

### 5.2.2. Block Orientation

[33] The blocks show different long-axis orientations, as illustrated by the rose diagrams on Figure 8d. In zone 1, long-axis orientations are variable and no predominant directions are evident. They predominantly occur along two northwest trending patches away from the diapir axis. In



zone 2, there is a preferential northwest trending orientation for the majority of the blocks. This is particularly evident on the flanks of diapir D3 where the larger blocks tend to show the long axis oriented toward northwest directions. A similar northwest trend for the majority of mapped blocks is observed in zone 3, with a secondary west-east trend. In zone 2 there is clear general orientation of the blocks around the flanks of the salt diapirs which tends to be parallel to the diapir axis line, whereas in the nonpierced zone 3 their orientation is more varied (Figure 8d). The orientation of the blocks is commonly used as a diagnostic element for how far they have traveled in relation to the original location. In this study, the blocks show a predominant northwest trending orientation along the salt ridge, which suggests a similar dynamic and proximity to the source. Furthermore, the orientation also supports the hypothesis that Palaeogene faults and blocks are related as both features show similar trends in the rose diagrams.

**5.2.3. Block Density**

[34] Block density is shown to vary within each zone in relation to the distance to the diapir axis. The graph in Figure 9b shows the lowest number of block occurrences close to the center and rims of the diapiric ridge. In essence, the majority of the blocks in MTD-A1 are within distances ranging from four to ten kilometres west of the diapir axis. In contrast, the central section registers the lowest density, especially within the first two kilometres west of the reference line.

[35] Comparing Figure 9b with the isochron map for MTD-A1 in Figure 4b, lower block density corresponds to a thinner area in zone 2, but in contrast it matches with some of the thickest intervals in zone 1. On the eastern flank, most of the blocks are located within zone 2, while the majority of them in zone 1 are limited to an area stretching just 4 kilometers away from the diapir ridge axis (Figure 9b). The density plot adds a quantitative aspect to the observations made in previous sections of this study about the block distribution within the MTD, especially their preferential northwest trending accumulation flanking the axis of the diapir ridge (Figure 4).

**5.2.4. Block Height**

[36] Measured blocks showed a relatively large range in height, generally limited by the thickness of MTD-A1. The majority of the blocks have heights between 100 and 180 m (Figure 9c), and are preferentially clustered in two main regions. On the west flank, the majority of the blocks are

**Figure 9.** Graphic representation of the statistical data obtained from the interpreted blocks in MTD-A1, showing evidence of their properties in the three different zones and distance to the diapir ridge axis. Bars on right-hand side represent the minimum, maximum and average values of each parameter at a given zone. (a) Block area distribution in the salt ridge. (b) Block density and their distance to the salt ridge axis. (c) Block height. (d) Width and length of blocks. (e) Width-length ratio of blocks in relation to their distance to the salt ridge axis. Blocks are distributed asymmetrically in relation to the ridge axis. The results show a general similarity of blocks along slope, indicating similar genesis and remobilization in the three studied regions.

located between 4 and 8 km from the salt diapir axis along the whole slope, regardless of which zone they are present. Outside this interval, the highest blocks closer to the central axis are located in zone 2, whereas in zone 3 tall blocks are found toward the limit of MTD-A1. The eastern side has the major agglomeration 4 km away from the axis line, with the majority of blocks in zone 1 also occurring within this region. The highest blocks on each flank of the salt anticline are generally located within the distances previously specified, reaching heights between 200 and 250 m high. Despite having quite significant height ranges, average values around 130 m were observed for each of the three main zones.

[37] The height, as the area, is another property to take in account when assessing how far the rafted blocks have traveled as this parameter tends to decrease with distance [Alves and Cartwright, 2009; Gee *et al.*, 2005; Laberg and Vorren, 2000]. In this study the highest elements are observed in the more centralized regions of MTD-A1 which also coincide with the thickest accumulations observed in the isochron map (Figure 4b). The fact that the highest elements tend to be in the central regions of the MTD also provide indications of any prefailure relief. The block height is commonly the same as the total MTD thickness, as shown in Figures 3 and 8.

### 5.2.5. Width/Length Ratio

[38] Variations in block dimensions, namely width and length, are represented in Figure 9d. The majority of the measurements are clustered within length values of 400 to 800 m and widths of 200 to 600 m. Outside this cluster, most of the remaining blocks have around 900 to 1200 m in length and reach up to 900 m in width, although blocks of zone 2 have lengths up to about 2400 m. Some of the highest block width/length values are located in zone 3, where they exceed 1000 m both in width and length. The residuals in Figure 9d were calculated to assess the fit of the observed values with the estimated values calculated by the linear trend. The residuals plot shows the regression against length values. The even distribution for residual values confirms the linear relation between block width and length.

[39] Comparing the width-to-length ratio with the position within the salt ridge, there is no evident distinction between the subzones or the distance from the reference axis (Figure 9d). The ratio values range from 0.2 to close to 1 across most of the block area in MTD-A1, except for the western limit where the ratio does not exceed 0.7. On the basis of the obtained values, the general shape ratio of the blocks does not seem to vary significantly along the slope, as average w/l ratios of 0.60 are seen in zones 1 and 2, and of 0.65 in zone 3. This aspect ratio of the blocks is commonly related to the degree of disaggregation, and consequently with their breakdown with transport [De Blasio *et al.*, 2006]. Many blocks show width/length ratios with high values, which can be interpreted as being relatively close to their source.

## 5.3. Block Deformation

### 5.3.1. Deformation Styles

[40] The studied remnant blocks show distinct styles of deformation. We classified these in three types, each related to a style of block deformation observed on the seismic

profiles (Figure 10). Minor deformation blocks preserve the original stratal relations, shown by packages of parallel subhorizontal reflections, often subparallel to strata present in unit 1 (Figure 10a). The moderate deformation type includes tilted blocks which show diverging dips in internal strata, as well as internal folds (Figure 10b). These folds are more common in larger blocks. The folding is mostly materialized as antiforms, although some synforms are observed. Major deformation show internal strata dips over 15 degrees (Figure 10c), frequently with internal folding. It is common to find blocks with major deformation in contact either with the same or the other deformation styles. Boundaries of observed blocks are well marked, and commonly coincide with faults underlying MTD-A1. Their contacts often suggest that they derive from the breakup of a larger block (Figure 3e). The deformation of the blocks will imply different degrees of fracturing and folding within them, especially as smaller scale features.

### 5.3.2. Quantification and Distribution of Deformation Types

[41] In this section we show a quantified analysis of the different types of block deformation. Figure 10d shows the distribution of the blocks within each established zone, as well as their position in relation to the salt diapirs. The distribution is not uniform, with the three styles of block deformation commonly occurring together. The general models for flow transformation for MTDs state that there is a gradual increase in block deformation toward the distal regions [Homza, 2004], but our results show contrasting results with different degrees of deformation occurring at the same locations. The distributions of each deformation style in relation to the axis of the main salt ridge are shown in Figure 10e. The eastern flank has fewer blocks, comprising 48 of the total 172, with the majority located in zone 2. Moderately deformed blocks are the most common found through the extension of this flank, and these also constitute most of the ones identified in zone 1. Blocks of minor deformation in zone 2 show higher densities close to the diapir axis and in distances over 6 km away from it, with low occurrences in between (Figure 10e).

[42] On the western flank, the amount of blocks is much higher and their distribution is less uniform, tending to be clustered. Zone 1 has the simplest distribution with the blocks roughly aligned along a limited area. Zones 2 and 3 tend to show similar clustering and distribution trends. In each of the subzones blocks of minor and moderate deformation occur relatively mixed within the same locations, although in zone 2 the latter type tends to occur further from the diapir axis (Figure 10d). As for the major deformation blocks, there is an evident higher number of these toward the rims of MTD-A1, especially toward the west. Nevertheless, major deformation blocks are also found in close relation with minor deformation ones in the main clusters observed above the diapir ridge (Figures 2, 3d, 5b, 7d, and 10d).

[43] The average values for the width/length ratio, as well as the number and proportion of deformed blocks are summarized in Table 1. In zone 1 the majority of blocks have moderate deformation which also corresponds to the blocks with the highest average areas and heights, but in terms of width/length ratio they are similar to the major deformation style. As for zone 2, the proportion of each

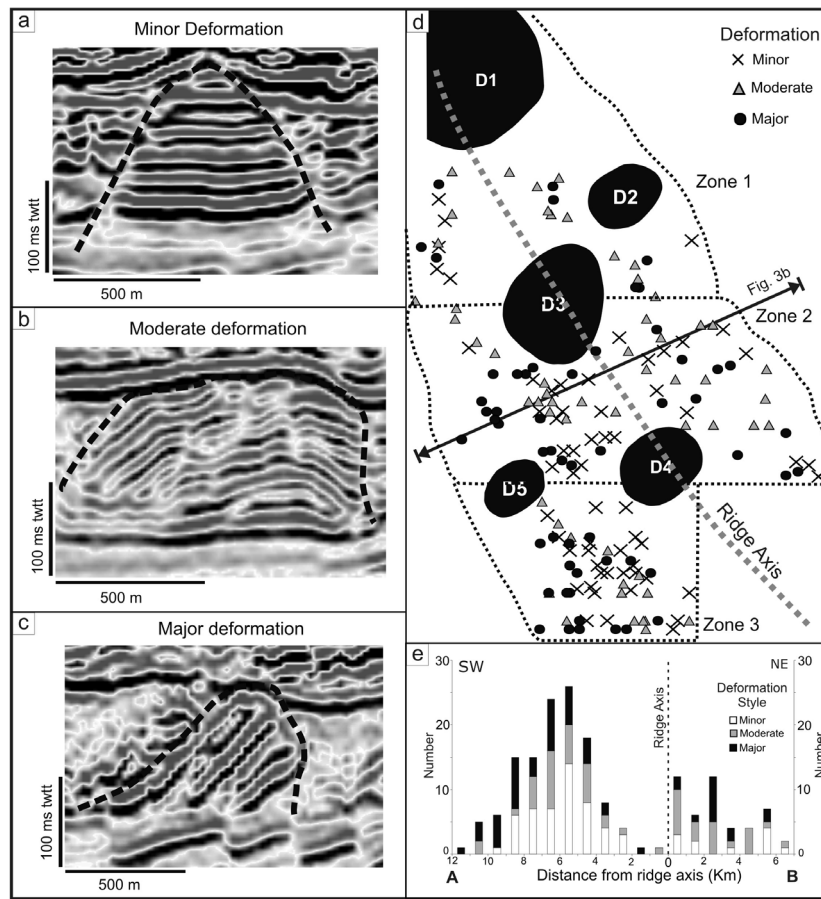


**Figure 10.** Different styles of block deformation. (a) Minor deformation represented by subhorizontal internal strata. (b) Moderate deformation with folding and low tilt of blocks. (c) Major deformation, represented by steeply dipping strata due to block rotation. (d) Distribution of block deformation styles along the salt ridge. (e) Graph of the frequency of deformation styles in relation to the distance from the ridge axis. The plot in Figure 10e is a projection of the blocks distribution shown in Figure 10d, and no zone distinction is represented. Note the relatively uniform distribution of deformation styles, with the exception of the western rim of the MTD where major deformation is prevalent.

deformation style is similar. In terms of height values, the highest averages are for minor deformation, reaching up to 153 m, with the remaining being around 125 m. The blocks with major deformation cover larger areas, with an average value of 0.43 km<sup>2</sup>, nearly twice the average area of the two other types. Minor deformation blocks are the most abundant in zone 3, representing 45.3% of the total. This is followed by major deformation blocks (31.25%) and lastly by 23.44% of the moderate style. Contrasting with the latter values, the moderately deformed blocks have the highest

average values for height (91.4 m) and area (0.58 km<sup>2</sup>). As for the width/length ratios, all of them have similar values and as such relatively similar shapes.

**6. Discussion**

**6.1. Halokinetic Structures as Triggers of Slope Instability**

[44] The results in this paper show an unusual relation between MTDs and halokinetic structures, as the thickest

**Table 1.** Average Values of Blocks Properties According to Style of Deformation and Slope Zone

Deformation	Zone 1					Zone 2					Zone 3				
	W/L Ratio	Area (km <sup>2</sup> )	Height (m)	Nr	Percentage	W/L Ratio	Area (km <sup>2</sup> )	Height (m)	Nr	Percentage	W/L Ratio	Area (km <sup>2</sup> )	Height (m)	Nr	Percentage
Style 1	0.51	0.33	72.67	6	21.4%	0.64	0.26	98.92	26	32.5%	0.64	0.32	88.72	29	45.3%
Style 2	0.63	0.40	96.00	14	50.0%	0.63	0.26	80.67	27	33.8%	0.68	0.58	91.4	15	23.4%
Style 3	0.64	0.32	80.50	8	28.6%	0.54	0.43	81.11	27	33.8%	0.65	0.26	79.2	20	31.3%

accumulations of remnant/rafted strata occur within the region of salt growth, with MTD-A1 thinning away into the salt withdrawal basins (Figures 2 and 5). This character contrasts with most published examples, which show accumulation and thicker deposits within salt withdrawal basins, and thinning on the rims of diapirs due to sediment removal [Alves and Cartwright, 2009; McAdoo et al., 2000; Tripsanas et al., 2004]. Consequently, the principal question rising from our observations regards the origin and flow dynamics of MTD-A1. In this discussion are presented two distinct hypotheses regarding long and short travel distances of the mass flows.

[45] A first explanation is that MTD-A1 originated from a failure upslope from the study area, flowing southeast along a depocenter approximately coincident with the regions where the thickest accumulations (and the majority of the blocks) are observed. The blocks within the failed strata would flow and accumulate in downslope locations, as in zone 3. This implies limited, if any, salt growth at the time of the MTD deposition. We must consider that for such long runout the blocks would suffer size reduction and reorientation along the extension of the flow [Alves and Cartwright, 2009; Bull et al., 2009; Homza, 2004; Laberg and Vorren, 2000]. The interpreted seismic data do not support this interpretation, as block with similar geometries were observed in the three studied zones. In addition, this explanation implies that any alignment between rafted blocks and underlying faults would be aleatory. The various examples illustrated in the seismic profiles suggest a closer link between underlying faults and remnant/rafted blocks as evidenced, for instance, by the presence of remnant strata over crestal faults (Figures 2, 3, and 8).

[46] A second explanation includes complex multidirectional remobilization of MTD-A1, with shorter travel distances involved and a localized origin for the blocks. The thickness and attribute data in Figure 4, depicting the location of remnant/rafted blocks, suggest a nearly mirror distribution of the MTD features relatively to the diapir axis. Statistical results confirm the latter statement as blocks cluster within specific distances to the diapir axis, and tend to show a gradual decrease in size toward the rims of the salt ridge (Figure 10). This suggests remobilization of material from the central parts of the salt ridge toward its margins. Furthermore, high values of the block width-length ratio are indicative of proximity to the source regions, i.e., short remobilization distance, being this particularly evident for zone 3 (Figure 10e).

[47] Short remobilizations are also supported by the close spacing of blocks and their relation to underlying faults. This is particularly noted in the case of fault-bounded blocks observed on top of the ridges and in interdiapiric areas (Figure 3). Such failed blocks represent localized portions of prefailure strata segmented into several crestal fault blocks developed above growing salt structures [Cobbold and Szatmari, 1991; Gaullier and Vendeville, 2005]. In contrast, blocks not underlain by vertically propagating faults on the western part of the salt ridge imply a different origin and further travel distances comparatively to the fault-related ones, but their presence above the crests of the buried ridges does not rule out a salt-related origin (Figures 2 and 3). Blocks commonly develop in extensional domains of the MTD, whereas stratal imbrications and thrust fea-

tures characterize the compressional domains [Ashbranner et al., 2010]. On the upper slope (zone 1), the MTD imbrications evidence north derived flows (Figures 7b and 11d), but there is also a lateral (W-E) component derived from the collapse of strata over the upslope sections of ridge BR2 (Figures 7a and 11d). Notice also that this area is characterized by a steeper profile of Horizon 1 (Figure 4d).

[48] In the remaining zones, the flow dynamics can be estimated from the geometry of the blocks. The block rotation, orientation and proximity on western rim of zones 2 and 3 (Figures 1 and 6) delimit an eastward flowing compressional component of the MTD, with evidence of thrusting observed on the seismic profiles (Figures 2, 5, 7c, and 7d). Central regions of the MTD generally correlate with an extensional regime, as evidenced the dispersal and spacing of the blocks. The presence of rotated blocks close to less deformed ones may imply different downslope velocities within the flow, with the possibility of the increase of deformation being due to the collision of smaller, faster traveling blocks with larger ones with limited movement. Other possibility is that the more deformed blocks result from squeezing of softer material between less competent strata (Figure 7d). The latter is also supported by published works of onshore fossil MTDs that have documented the presence of both brittle and ductile block deformation occurring close together due to contrasting sediment cementation [Callot et al., 2008; Odonne et al., 2011]. This has also been associated with the block sedimentary composition, but there is no indicator that such could be the case in MTD-A1. In addition, the major deformation blocks might derive from the breakup and collapse of the flanks of larger ones.

[49] Such complex associations reveal how the classical models of intra-MTD deformation evolution may not be suitable to describe this and other complex failures. Combining the interpretations above, and the fact that low remobilization blocks occur within the thickest sections of the MTD, we estimate the presence of a palaeorelief developed along the diapir ridge (Figures 11a and 11e). The morphology of the gliding surface evidences some flattened or depressed regions (Figure 4a) which may contradict the presence of such relief, but this is either due to erosion (Figure 3c) or to limited subsidence of the faulted overburden due to the growth and eventual deflation on the crest of salt ridges (Figure 11f) [e.g., Dooley et al., 2009; Jackson et al., 1994; Schultz-Ela et al., 1993]. On seismic profiles this is evidenced by relatively flattened faulted sections of Horizon 1 (Figure 3). Consequently, MTD-A1 is interpreted to form due to the collapse of the relief created within the diapir ridge along the MTD basal shear surface (Figure 11). The differential movements observed are also concordant with the collapse of a previously folded morphology along an irregular basal surface with different dip directions. The central region of the diapir ridge shows short remobilization of the blocks, with suggested spreading and accumulation occurring perpendicularly to the axis of the main salt ridge (Figure 11d). A simultaneous collapse of the northern and western limits of the MTD imply a southward and eastward flow of failed strata, with the lateral collapses also involving the formation of back-tilted blocks and collision of these with the less remobilized central masses of the MTD (Figure 11g). Clustering of blocks is common within de-

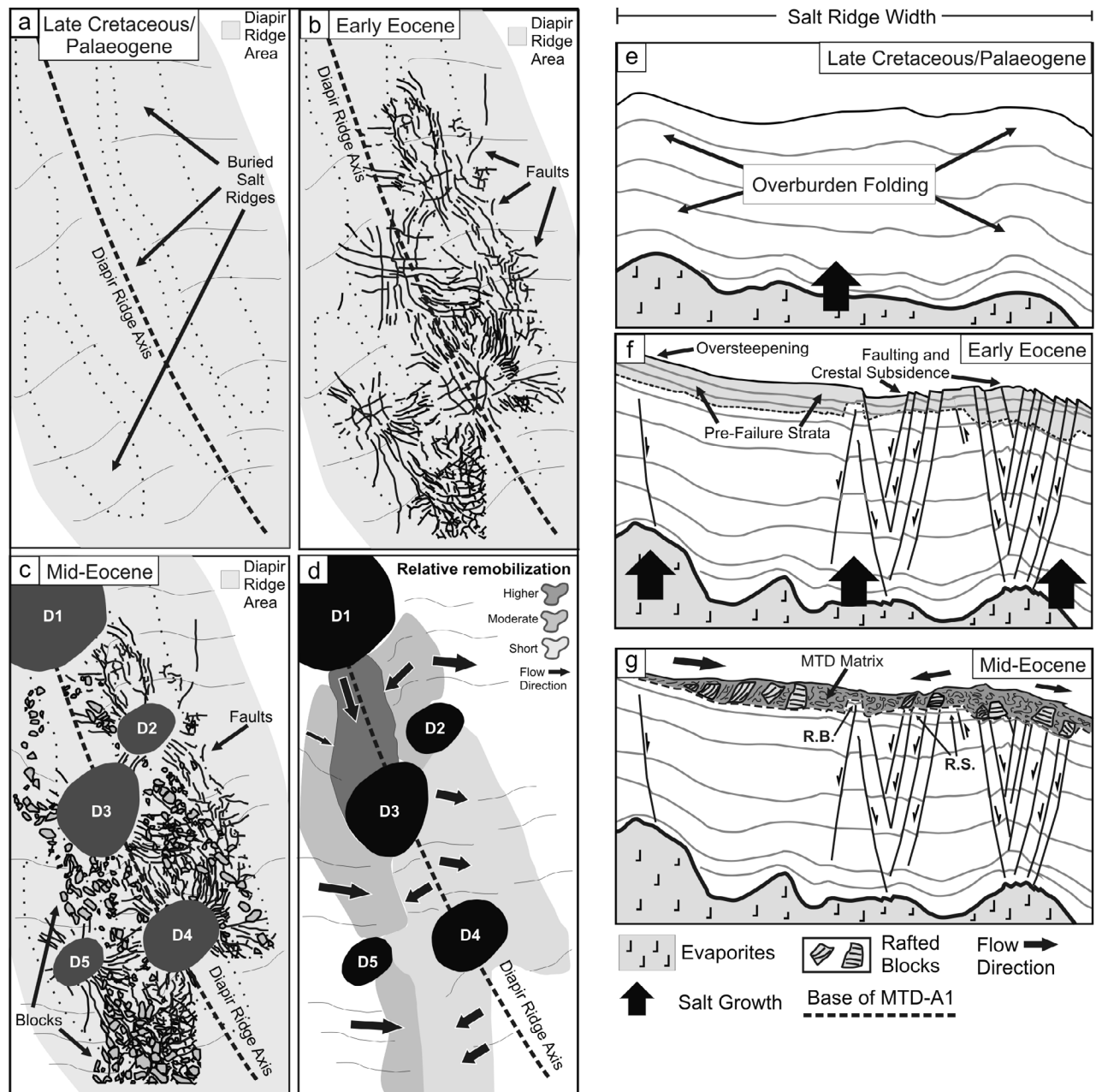


**Figure 11.** Schematic diagram with the evolution of the diapir ridge. (a and e) Salt ridges developed during the Late Cretaceous and Palaeogene, deforming the overburden and forming a northwest oriented relief. (b and f) Early Eocene deformation and faulting of the overburden along the buried salt ridges. Faulting at this stage also led to partial subsidence on the crest of the salt ridges and diapirs. (c and g) Mid-Eocene failure and deposition of MTD-A1 with numerous blocks located along the main diapir ridge. Remnant blocks/strata are limited by faults, whereas the presence of rafted blocks is not strictly dependant of underlying crestal faults. (d) Diagram illustrating the relative movement of the MTD components. Higher remobilization is interpreted to occur in the area north of diapir D3, with convergence of flow directions. Short remobilization is interpreted to have occurred along the axis of the diapir ridge, with MTD components spreading perpendicularly to the latter. Moderate remobilization occurred predominantly along the western rim of the MTD with these components flowing eastward, colliding with the ones in the central regions.

pressions created by crestral subsidence along buried salt ridges, or due to higher erosion in these deformed areas at the time of collapse (Figure 3), suggesting that their limits also restricted the transport of failed features. Thus, the failure of MTD-A1 is proposed to occur by faulting and oversteepening of the overburden due to the growth of the underlying salt diapirs. This interpretation is corroborated by (1) the close link between the blocks and preexisting faults and (2) the fact that the limits of the main diapir ridge are coincident with the limits of MTD-A1, particularly in regions when the failure scarps are underlain by salt ridges (Figures 2 and 3).

[50] Analogue complex failures identified in fossil MTDs show similar features to the one analyzed in this work, where block and matrix deformation provide indicators to assess flow movement and delimit different components [Alves and Lourenço, 2010; Butler and McCaffrey, 2010; Callot et al., 2008; Lucente and Pini, 2003; Lucente and Pini, 2008; Odonne et al., 2011]. When derived from distinct sources, often due to tectonically influenced topographic oversteepening and failure, the components are likely to exhibit both distinct lithological compositions and bulk deformation styles [e.g., Callot et al., 2008]. As the subseismic deformation often mimics large scale features [Callot et al., 2008], on-land slabs can be used to estimate smaller features present in submarine slide blocks. Plastic deformation features are represented by increasing fold vergence and internal strata disruption the higher the remobilization distance and shear intensity [Alves and Lourenço, 2010; Odonne et al., 2011]. Faulting is also observed at multiple scales, either derived from the initial failure or developed/enhanced with remobilization [Alves and Lourenço, 2010; Lucente and Pini, 2003; Odonne et al., 2011]. Increased complexity is often observed at the block base in the interface with the basal shear surfaces. The high shear stress leads to increased brecciation and soft sediment deformation at these zones of variable thickness [Alves and Lourenço, 2010], leading the formation of clastic injectites propagating upwards the failed material (block or matrix) resultant from expulsion of overpressurized fluids within the sediment [Butler and McCaffrey, 2010; Callot et al., 2008; Odonne et al., 2011]. Nevertheless, these features are less expected to occur in remnant blocks as these were not remobilized and are not underlain by any shear surface.

[51] The analogy between MTD-A1 and fossil landslides strengthens the importance of integrating geophysical and land based methods to improve the characterization of such deposits. While field data provides details of small to mesoscale features and complexity, seismic data allows wider-scale morphological and structural interpretations where the sole study of outcrops shows limitations.

## 6.2. Can Blocks Form Preferential Fluid Flow Paths?

[52] The studied blocks represent strata that maintain some or most of its original cohesion and constitute potentially permeable conduits for fluid flow through MTD-A1. Lithologic or structural features below seismic resolution, as thin permeable layers or fault networks, must also be considered as these can be as efficient fluid pathways as the larger seismically resolved features within the observed blocks.

[53] The examples in our study show faulting not only of unit 1 but also evidence internal fractures in blocks (Figure 3). The presence of such damage zone can lead to an enhancement of the permeability potential close to faults, within or below the blocks. Considering that the blocks could form effective vertical bypass mechanisms through the MTD, the identification of the major clusters may also indicate areas with potential higher rates of leakage. The plots of blocks distribution show the accumulations to be located between four and eight kilometres on the western flank of the diapir axis, and in the first two kilometres on the eastern flank (Figure 9).

[54] Block height is a relevant property to take into account as it sets the vertical extension of the permeable areas. Despite the range of values, the average height is around 150 m (Figure 9c), which is also the average thickness of the MTD. The highest blocks show minor and moderate deformation therefore we also expect a better preservation of the internal strata along the major bypass points (Table 1). One of the issues that may arise is how can fluid flow through the MTD basal shear surfaces where the rafted blocks rest, which are commonly more compacted [Sawyer et al., 2009], and the erosive surface itself can form a permeability barrier [Allan et al., 2006]. The remnant blocks constitute an exception as these are expected to show vertical stratigraphic continuity with the underlying strata. In this case, any permeable features within the remnant blocks are not interrupted and this can lead to the supply of fluids through, and toward the top of, the MTD. The importance of faults and blocks on the bypass of MTD basal surfaces is evidenced in our data as several amplitude anomalies are present in the studied stratigraphic units (Figure 12). These anomalies are interpreted to be fluid-related as they are represented by local amplitude increases typical of bright spots [Løseth et al., 2009; Sheriff and Geldart, 1995] and occur in stratigraphic intervals with proven presence of hydrocarbons [Biassussi et al., 1998]. Bright spots are frequent in the vicinities of the crestral faults developed in Palaeogene strata (Figure 12a), confirming their importance in fluid flow paths in the Espirito Santo Basin [Biassussi et al., 1998]. In regions of the MTD underlain by faults, but where blocks are absent, fluid accumulates along the basal surface retained by the low permeability debrites (Figures 12b and 12c). On the contrary, when fault-bounded blocks are present they can establish vertical migration paths either through their internal strata, or along the block-debrite interface (Figures 11a and 11e). Moreover, fault intersections are potential points for increased rates of fluid leakage [Gartrell et al., 2004; Ligtenberg, 2005]. Strikingly, in our study the higher amount of intersections is observed in zone 3 and the eastern area of zone 2 (Figure 8). This gets additional relevance as the faulted sections of unit 1 are predominantly located on the flanks of the developed diapirs and above the crest of buried salt diapirs and ridges, which are documented to be locations of important fluid leakage in sedimentary basins [e.g., Cartwright et al., 2007; Ligtenberg, 2005; Meldahl et al., 2001].

[55] Taking these factors into consideration, we establish a differential permeability potential for distinct regions of the MTD (Figure 12d). The highest permeability potential is observed in areas with the closer relations between the blocks and the faults, especially when the blocks are

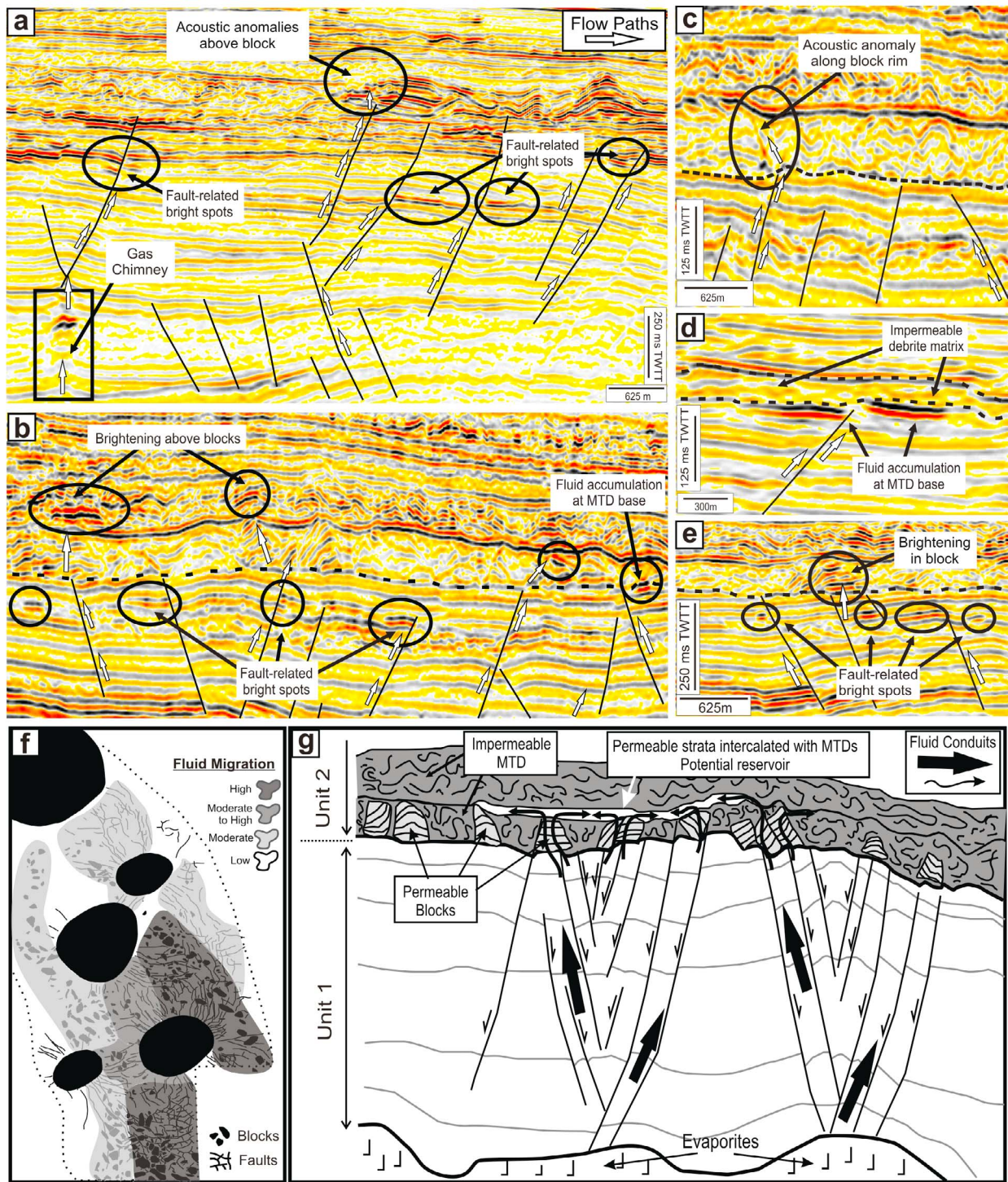


**Figure 12.** (a–e) Acoustic anomalies in the seismic data evidence the presence of fluids in the studied strata. Faults in unit 1 are associated with fluid migration, sourced from Late Cretaceous strata. Brightening in or above fault-bounded blocks, or the block matrix contact suggest permeability enhancement features within the MTD. When blocks are absent, fluids are trapped underneath the impermeable debris. (f) Diagram representing the fluid flow potential within MTD-A1. Areas with higher block frequency and faults have higher potential, whereas areas where no blocks or faults are observed have the lowest. Moderate potential is expected in faulted regions with fewer blocks, or where blocks show no evident relation to underlying faults. (g) Schematic drawing representing fluid bypass through MTD units suggested by the close relation of faults and remnant/rafted blocks. Faults act as vertical fluid conduits in prefailure strata. Migration through the MTD is made along permeable strata and fractures in the blocks.

delimited or cut by faults (Figure 3). This also corresponds to the sections where the blocks area and height have the larger values (Figure 10). Regions of moderate flow potential are established to include blocks that do not show any evident relation with underlying faults, exemplified by the western limit of the MTD in zones 1 and 2. The lowest permeability potential is expected along the diapir axis where no blocks of faults are observed (central zone 1). In general, the faults are truncated by the erosive surface of the MTD, nevertheless, there is an exception on the northern flank of diapir D2 (zone 1). Here major crestal faults cut through MTD-A1 and overlying strata (Figure 7a), thus constituting a major fault-based bypass point to the strata in unit 2. In addition, we can correlate the permeability zonation of the MTD with the different flow components discussed above. As such, the higher permeability regions are suggested to relate to the MTD sections that show lower remobilization in relation to their source, with the permeability potential tending to decrease as the transport distance increases. Furthermore, fluid expulsion can also occur at the interface between MTD components with colliding flow behaviors (e.g., western and central regions of MTD-A1) [Lucente and Taviani, 2005]. Even in the case of short-period postdepositional expulsion, resulting fluidization structures created along the contact area could allow flow of posterior fluids supplied to the MTD.

[56] To summarize, the relation of the studied blocks in MTD-A1 with the Palaeogene faults in unit 1 (Figure 3) establishes a potential hydrocarbon flow mechanism through the otherwise low permeability MTDs. This provides a viable process to supply reservoir prone lithologies above the mass wasting products (Figure 12e), also allowing for fluids to accumulate within the MTDs if the adequate lithologies are present [Beaubouef and Abreu, 2010; Galloway, 1998; Welbon et al., 2007]. In fact, the internal deformation in MTD-A1 is likely to be more intense than what is observed on seismic data as faults are also commonly surrounded by subseismic scale damage zones [e.g., Knipe et al., 1998; Zhang et al., 2010]. Outcrop- and core-based studies have also shown the degree of complex brittle and ductile deformation within MTDs and these can replicate at variable scales [Callot et al., 2008]. The development of microfractures is common in these deposits [Tripsanas et al., 2008], especially in higher cohesion sediments. Fractures within rafted blocks commonly develop upon the initial failure [Alves and Lourenço, 2010] but the effects of shear stress during transport must also be considered, regardless of the travel distances, which can either enhance previous fracturing or develop new ones [Alves and Lourenço, 2010; Lucente and Pini, 2003]. This, associated with overpressure along the basal shear zone, favors the formation of clastic injectites propagating upwards either through the heterogeneous MTD matrix or tensile fractures in the block base [Alves and Lourenço, 2010; Butler and McCaffrey, 2010; Callot et al., 2008]. Clastic injectites are particularly important for smaller scale fluid flow within failed strata as they form good fluid conduits which can have higher permeability than their source beds [Odonne et al., 2011]. Furthermore, fractures propagating on top of the blocks can also be filled by postfailure permeable clastic material [Odonne et al., 2011]. The presence of sand either as a primary block component or derived from fracture filling favors the formation

of permeable paths through the block strata, which can be enhanced or hindered due to variable styles of block deformation.

## 7. Conclusions

[57] The detailed analysis of the earliest mid-Eocene mass wasting deposit (MTD-A1) in the Espírito Santo Basin revealed a marked internal heterogeneity. Thicker accumulations of MTD-A1 are located within the region underlain by developed salt ridges and diapirs, thinning toward the salt withdrawal basin, contrasting with the more common situation of stratal thinning above growing salt structures. Several remnant/rafted blocks were identified, evidenced by subparallel reflections bordered by chaotic patterns in the MTD. In essence, major conclusions from this paper are as follows:

[58] 1. The origin of the blocks is linked to extensive arrays of halokinetic-related faults that deformed the pre-failure strata. The close relation shown by the faults and blocks, complemented by MTD thickness maps, shows that the blocks occur close to their source area.

[59] 2. Blocks show, on average, heights of 150 m and areas of about 0.4 km<sup>2</sup>, with these values maintained down-slope, along the main ridge. This indicates similar processes and remobilisation of MTD-A1 at all slope locations. Three different styles of block deformation were identified. Failure and collapse of a pre-Eocene northwest trending relief generated a complex flow of the failed strata which spread along-slope in directions perpendicular to the diapir ridge axis. Relative block distribution also provides a way of dating the triggering of salt structures at the time of failure.

[60] The MTD heterogeneities shown in this paper have implications in the assessment of the internal properties of failed strata and can constitute permeable fluid conduits, especially when in close relation with underlying faults. This is crucial when estimating seal capacity and/or fluid pathways in hydrocarbon exploration areas. The results shown for the Espírito Santo Basin in Brazil can be applied and compared to other continental margins with important mass wasting.

[61] **Acknowledgments.** The authors are grateful to CGG-Veritas for the permission conceded to publish this research paper. Schlumberger is acknowledged for the provision of seismic interpretation software. Davide Gamboa thanks the Fundação para a Ciência e a Tecnologia (FCT) for the SFRH/BD/38819/2007 Ph.D. grant. The authors thank W. Mohriak and two anonymous reviewers for their constructive comments that greatly improved the final manuscript.

## References

- Allan, J. R., S. Q. Sun, and R. Trice (2006), The deliberate search for stratigraphic and subtle combination traps: Where are we now?, *Geol. Soc. Spec. Publ.*, 254, 57–103.
- Alves, T. M. (2010), 3D Seismic examples of differential compaction in mass-transport deposits and their effect on post-failure strata, *Mar. Geol.*, 271(3–4), 212–224, doi:10.1016/j.margeo.2010.02.014.
- Alves, T. M., and J. A. Cartwright (2009), Volume balance of a submarine landslide in the Espírito Santo Basin, offshore Brazil: Quantifying sea-floor erosion, sediment accumulation and depletion, *Earth Planet. Sci. Lett.*, 288(3–4), 572–580, doi:10.1016/j.epsl.2009.10.020.
- Alves, T. M., and S. D. N. Lourenço (2010), Geomorphologic features related to gravitational collapse: Submarine landsliding to lateral spreading on a Late Miocene-Quaternary slope (SE Crete, eastern Mediterranean), *Geomorphology*, 123(1–2), 13–33, doi:10.1016/j.geomorph.2010.04.030.

- Alves, T. M., J. Cartwright, and R. J. Davies (2009), Faulting of salt-withdrawal basins during early halokinesis: Effects on the Paleogene Rio Doce Canyon system (Espírito Santo Basin, Brazil), *AAPG Bull.*, 93(5), 617–652, doi:10.1306/02030908105.
- Armitage, D. A., B. W. Romans, J. A. Covault, and S. A. Graham (2009), The influence of mass-transport-deposit surface topography on the evolution of turbidite architecture: The Sierra Contreras, Tres Pasos Formation (Cretaceous), southern Chile, *J. Sediment. Res.*, 79(5), 287–301, doi:10.2110/jsr.2009.035.
- Ashabraner, L. B., E. K. Tripsanas, and R. C. Shipp (2010), Multi-direction flow in a mass-transport deposit, Santos Basin, offshore Brazil, in *Submarine Mass Movements and Their Consequences*, edited by D. C. Mosher et al., pp. 247–255, Springer, New York, doi:10.1007/978-90-481-3071-9\_20.
- Barker, P. F., R. T. Buffler, and L. A. Gambôa (1983), A seismic reflection study of the Rio Grande rise, *Deep Sea Drill. Program Initial Rep.*, 72, 953–976.
- Baudon, C., and J. Cartwright (2008), The kinematics of reactivation of normal faults using high resolution throw mapping, *J. Struct. Geol.*, 30(8), 1072–1084, doi:10.1016/j.jsg.2008.04.008.
- Beaubouef, R. T., and V. Abreu (2010), MTCs of the Brazos-Trinity Slope System; Thoughts on the sequence stratigraphy of MTCs and their possible roles in shaping hydrocarbon traps, in *Submarine Mass Movements and Their Consequences*, edited by D. C. Mosher et al., pp. 475–490, Springer, New York, doi:10.1007/978-90-481-3071-9\_39.
- Biassussi, A. S., R. S. F. D'Avila, A. C. Guirro, and J. G. R. Silva (1998), Urucutuca-Urucutuca(?) petroleum system, Espírito Santo Basin, Brazil, paper presented at AAPG International Conference and Exhibition, Rio de Janeiro, Brazil.
- Brown, A. R. (2004), *Interpretation of Three-Dimensional Seismic Data*, 6th ed., Am. Assoc. of Pet. Geol., Tulsa, Okla.
- Bull, S., J. Cartwright, and M. Huuse (2009), A review of kinematic indicators from mass-transport complexes using 3D seismic data, *Mar. Pet. Geol.*, 26(7), 1132–1151, doi:10.1016/j.marpetgeo.2008.09.011.
- Butler, R. W. H., and W. D. McCaffrey (2010), Structural evolution and sediment entrapment in mass-transport complexes: Outcrop studies from Italy, *J. Geol. Soc.*, 167(3), 617–631, doi:10.1144/0016-76492009-041.
- Callot, P., F. Odonne, and T. Sempere (2008), Liquefaction and soft-sediment deformation in a limestone megabreccia: The Ayabacas giant collapse, Cretaceous, southern Peru, *Sediment. Geol.*, 212(1–4), 49–69, doi:10.1016/j.sedgeo.2008.10.006.
- Canals, M., et al. (2004), Slope failure dynamics and impacts from seafloor and shallow sub-seafloor geophysical data: Case studies from the COSTA project, *Mar. Geol.*, 213(1–4), 9–72, doi:10.1016/j.margeo.2004.10.001.
- Cartwright, J., M. Huuse, and A. Aplin (2007), Seal bypass systems, *AAPG Bull.*, 91(8), 1141–1166, doi:10.1306/04090705181.
- Cobbold, P. R., and P. Szatmari (1991), Radial gravitational gliding on passive margins, *Tectonophysics*, 188(3–4), 249–289, doi:10.1016/0040-1951(91)90459-6.
- Davison, I. (1999), Tectonics and hydrocarbon distribution along the Brazilian South Atlantic margin, in *The Oil and Gas Habitats of the South Atlantic*, edited by N. R. Cameron, R. H. Bate, and V. S. Clure, *Geol. Soc. Spec. Publ.*, 153, 133–151.
- Davison, I. (2004), Bathymetric control on Paleocene gravity flows around salt domes in the Central Graben, North Sea, in *Salt-Sediment Interactions and Hydrocarbon Prospectivity: Concepts, Applications, and Case Studies for the 21st Century*, edited by P. J. Post et al., pp. 1031–1144, Gulf Coast Sect., Soc. of Sediment. Geol., Houston, Tex.
- Davison, I. (2007), Geology and tectonics of the South Atlantic Brazilian salt basins, in *Deformation of the Continental Crust: The Legacy of Mike Coward*, edited by A. C. Ries, R. W. H. Butler, and R. H. Graham, *Geol. Soc. Spec. Publ.*, 272, 345–359.
- Davison, I., I. Alsop, and D. Blundell (1996), Salt tectonics: Some aspects of deformation mechanics, in *Salt Tectonics*, edited by G. I. Alsop, D. J. Blundell, and I. Davison, *Geol. Soc. Spec. Publ.*, 100, 1–10.
- Davison, I., G. I. Alsop, N. G. Evans, and M. Safaricz (2000a), Overburden deformation patterns and mechanisms of salt diapir penetration in the Central Graben, North Sea, *Mar. Pet. Geol.*, 17(5), 601–618, doi:10.1016/S0264-8172(00)00011-8.
- Davison, I., I. Alsop, P. Birch, C. Elders, N. Evans, H. Nicholson, P. Rorison, D. Wade, J. Woodward, and M. Young (2000b), Geometry and late-stage structural evolution of Central Graben salt diapirs, North Sea, *Mar. Pet. Geol.*, 17(4), 499–522, doi:10.1016/S0264-8172(99)00068-9.
- De Blasio, F. V., L. E. Engvik, and A. Elverhøi (2006), Sliding of outrunner blocks from submarine landslides, *Geophys. Res. Lett.*, 33, L06614, doi:10.1029/2005GL025165.
- Demercian, S., P. Szatmari, and P. R. Cobbold (1993), Style and pattern of salt diapirs due to thin-skinned gravitational gliding, Campos and Santos basins, offshore Brazil, *Tectonophysics*, 228(3–4), 393–433, doi:10.1016/0040-1951(93)90351-J.
- Deptuck, M. E., Z. Sylvester, C. Pirmez, and C. O'Byrne (2007), Migration-aggradation history and 3-D seismic geomorphology of submarine channels in the Pleistocene Benin-major Canyon, western Niger Delta slope, *Mar. Pet. Geol.*, 24(6–9), 406–433, doi:10.1016/j.marpetgeo.2007.01.005.
- Dooley, T. P., M. P. A. Jackson, and M. R. Hudec (2009), Inflation and deflation of deeply buried salt stocks during lateral shortening, *J. Struct. Geol.*, 31(6), 582–600, doi:10.1016/j.jsg.2009.03.013.
- Dunlap, D. B., L. J. Wood, C. Weisenberger, and H. Jabour (2010), Seismic geomorphology of offshore Morocco's east margin. Safi Haute Mer area, *AAPG Bull.*, 94(5), 615–642, doi:10.1306/10270909055.
- Fiduk, J. C., E. R. Brush, L. E. Anderson, P. B. Gibbs, and M. G. Rowan (2004), Salt deformation, magmatism, and hydrocarbon prospectivity in the Espírito Santo Basin, offshore Brazil, in *Salt-Sediment Interactions and Hydrocarbon Prospectivity: Concepts, Applications, and Case Studies for the 21st Century*, edited by P. J. Post et al., pp. 370–392, Gulf Coast Sect., Soc. of Sediment. Geol., Houston, Tex.
- França, R. L., A. C. Del Rey, C. V. Tagliari, J. R. Brandão, and P. R. Fontanelli (2007), Bacia de Espírito Santo, *Bol. Geociênc. Petrobras*, 15(2), 501–509.
- Frey-Martinez, J., J. Cartwright, and D. James (2006), Frontally confined versus frontally emergent submarine landslides: A 3D seismic characterisation, *Mar. Pet. Geol.*, 23(5), 585–604, doi:10.1016/j.marpetgeo.2006.04.002.
- Galloway, W. E. (1998), Siliciclastic slope and base-of-slope depositional systems; Component facies, stratigraphic architecture and classification, *AAPG Bull.*, 82(4), 569–595.
- Gamboa, D., T. Alves, J. Cartwright, and P. Terrinha (2010), MTD distribution on a 'passive' continental margin: The Espírito Santo Basin (SE Brazil) during the Palaeogene, *Mar. Pet. Geol.*, 27(7), 1311–1324, doi:10.1016/j.marpetgeo.2010.05.008.
- Gartrell, A., Y. Zhang, M. Lisk, and D. Dewhurst (2004), Fault intersections as critical hydrocarbon leakage zones: Integrated field study and numerical modelling of an example from the Timor Sea, Australia, *Mar. Pet. Geol.*, 21(9), 1165–1179, doi:10.1016/j.marpetgeo.2004.08.001.
- Gaulhier, V., and B. C. Vendeville (2005), Salt tectonics driven by sediment progradation: Part II—Radial spreading of sedimentary lobes prograding above salt, *AAPG Bull.*, 89(8), 1081–1089, doi:10.1306/03310503064.
- Gee, M. J. R., R. L. Gawthorpe, and J. S. Friedmann (2005), Giant striations at the base of a submarine landslide, *Mar. Geol.*, 214(1–3), 287–294, doi:10.1016/j.margeo.2004.09.003.
- Gee, M. J. R., R. L. Gawthorpe, and S. J. Friedmann (2006), Triggering and evolution of a giant submarine landslide, offshore Angola, revealed by 3D seismic stratigraphy and geomorphology, *J. Sediment. Res.*, 76(1), 9–19, doi:10.2110/jsr.2006.02.
- Giles, K. A., and T. F. Lawton (2002), Halokinetic sequence stratigraphy adjacent to the El Papalote diapir, northeastern Mexico, *AAPG Bull.*, 86(5), 823–840.
- Guardado, L. R., L. A. P. Gamboa, and C. F. Luchesi (1989), Petroleum geology of the Campos Basin, a model for a producing Atlantic-type basin, *AAPG Mem.*, 48, 3–79.
- Guardado, L. R., A. R. Spadini, J. S. L. Brandão, and M. R. Mello (2000), Petroleum system of the Campos Basin, Brazil, *AAPG Mem.*, 73, 317–324.
- Homza, T. X. (2004), A structural interpretation of the Fish Creek Slide (Lower Cretaceous), northern Alaska, *AAPG Bull.*, 88(3), 265–278, doi:10.1306/10270303029.
- Hudec, M. R., and M. P. A. Jackson (2007), Terra infirma: Understanding salt tectonics, *Earth Sci. Rev.*, 82(1–2), 1–28, doi:10.1016/j.earscirev.2007.01.001.
- Illstad, T., F. V. De Blasio, A. Elverhøi, C. B. Harbitz, L. Engvik, O. Longva, and J. G. Marr (2004), On the frontal dynamics and morphology of submarine debris flows, *Mar. Geol.*, 213(1–4), 481–497, doi:10.1016/j.margeo.2004.10.020.
- Jackson, M. P. A., and M. R. Hudec (2005), Stratigraphic record of translation down ramps in a passive-margin salt detachment, *J. Struct. Geol.*, 27(5), 889–911.
- Jackson, M. P. A., and B. C. Vendeville (1994), Regional extension as a geologic trigger for diapirism, *Geol. Soc. Am. Bull.*, 106(1), 57–73, doi:10.1130/0016-7606(1994)106<0057:REAGT>2.3.CO;2.
- Jackson, M. P. A., B. Vendeville, and D. D. Schultz-Ela (1994), Structural dynamics of salt systems, *Annu. Rev. Earth Planet. Sci.*, 22, 93–117, doi:10.1146/annurev.ea.22.050194.000521.
- Jensen, J. L., P. W. M. Corbett, L. W. Lake, and D. J. Goggin (2007), *Statistics for Petroleum Geologists and Geoscientists, Handbook of Petroleum Exploration and Production 2*, 338 pp., Elsevier, New York.
- Knipe, R. J., G. Jones, and Q. J. Fisher (1998), Faulting, fault sealing and fluid flow in hydrocarbon reservoirs: An introduction, in *Faulting, Fault*

- Sealing and Fluid Flow in Hydrocarbon Reservoirs*, edited by G. Jones, Q. J. Fisher, and R. J. Knipe, *Geol. Soc. Spec. Publ.*, 147, 7–21.
- Laberg, J. S., and T. O. Vorren (2000), The Trænadjupet Slide, offshore Norway—Morphology, evacuation and triggering mechanisms, *Mar. Geol.*, 171(1–4), 95–114, doi:10.1016/S0025-3227(00)00112-2.
- Lee, C., J. A. Nott, and F. B. Keller (2004), Seismic expression of the Cenozoic mass transport complexes, deepwater Tarfaya-Agadir Basin, offshore Morocco, paper presented at Offshore Technology Conference, Houston, Texas.
- Ligtenberg, J. H. (2005), Detection of fluid migration pathways in seismic data: Implications for fault seal analysis, *Basin Res.*, 17(1), 141–153, doi:10.1111/j.1365-2117.2005.00258.x.
- Lima, C. (2003), Ongoing compression across South American plate: Observations, numerical modelling and some implications for petroleum geology, in *Fracture and In-Situ Stress Characterization of Hydrocarbon Reservoirs*, edited by M. Ameen, *Geol. Soc. Spec. Publ.*, 209, 87–100.
- Løseth, H., M. Gading, and L. Wensaas (2009), Hydrocarbon leakage interpreted on seismic data, *Mar. Pet. Geol.*, 26(7), 1304–1319, doi:10.1016/j.marpetgeo.2008.09.008.
- Lucente, C. C., and G. A. Pini (2003), Anatomy and emplacement mechanism of a large submarine slide within a Miocene foredeep in the northern Apennines, Italy: A field perspective, *Am. J. Sci.*, 303(7), 565–602, doi:10.2475/ajs.303.7.565.
- Lucente, C. C., and G. A. Pini (2008), Basin-wide mass-wasting complexes as markers of the Oligo-Miocene foredeep-accretionary wedge evolution in the northern Apennines, Italy, *Basin Res.*, 20(1), 49–71, doi:10.1111/j.1365-2117.2007.00344.x.
- Lucente, C. C., and M. Taviani (2005), Chemosynthetic communities as fingerprints of submarine sliding-linked hydrocarbon seepage, Miocene deep-sea strata of the Tuscan-Romagna Apennines, Italy, *Palaeogeogr. Palaeoclimatol. Palaeoecol.*, 227(1–3), 176–190, doi:10.1016/j.palaeo.2005.04.025.
- Masson, D. G., C. B. Harbitz, R. B. Wynn, G. Pedersen, and F. Løvholt (2006), Submarine landslides: Processes, triggers and hazard prediction, *Philos. Trans. R. Soc. A*, 364(1845), 2009–2039.
- McAdoo, B. G., L. F. Pratson, and D. L. Orange (2000), Submarine landslide geomorphology, US continental slope, *Mar. Geol.*, 169(1–2), 103–136, doi:10.1016/S0025-3227(00)00050-5.
- Meldahl, P., R. Heggland, B. Bril, and P. de Groot (2001), Identifying faults and gas chimneys using multiattributes and neural networks, *Leading Edge*, 20(5), 474–482, doi:10.1190/1.1438976.
- Mello, M. R., W. U. Mohriak, E. A. M. Koutsoukos, and G. Bacoccoli (1994), Selected petroleum systems in Brazil, in *AAPG Mem.*, 60, 499–512.
- Minisini, D., F. Trincardi, A. Asioli, M. Canu, and F. Fogliani (2007), Morphologic variability of exposed mass-transport deposits on the eastern slope of Gela Basin (Sicily channel), *Basin Res.*, 19(2), 217–240, doi:10.1111/j.1365-2117.2007.00324.x.
- Mohriak, W. U. (1995), Salt tectonics structural styles: Contrasts and similarities between the South Atlantic and the Gulf of Mexico, in *Salt, Sediment and Hydrocarbons*, edited by C. J. Travis et al., pp. 177–191, Gulf Coast Sect. of the Soc. of Econ. Paleontol. and Mineral., Houston, Tex.
- Mohriak, W. U. (2003), Bacias sedimentares da margem continental Brasileira, in *Geologia, Tectonica e Recursos Minerais do Brasil*, edited by L. A. Bizzi et al., pp. 87–165, Geol. Surv. of Brazil, Brasília.
- Mohriak, W. U. (2005), Interpretação geológica e geofísica da Bacia do Espírito Santo e da região de Abrolhos: Petrografia, datação radiométrica e visualização sísmica das rochas vulcânicas, *Bol. Geocienc. Petrobras*, 14(1), 133–142.
- Mohriak, W. U., M. R. Mello, J. F. Dewey, and J. R. Maxwell (1990), Petroleum geology of the Campos Basin, offshore Brazil, *Geol. Soc. Spec. Publ.*, 50, 119–141.
- Mohriak, W. U., J. H. L. Rabelo, R. D. De Matos, and M. C. De Barros (1995), Deep seismic reflection profiling of sedimentary basins offshore Brazil: Geological objectives and preliminary results in the Sergipe Basin, *J. Geodyn.*, 20(4), 515–539, doi:10.1016/0264-3707(95)00024-4.
- Mohriak, W. U., M. Nemcok, and G. Enciso (2008), South Atlantic divergent margin evolution: Rift-borded uplift and salt tectonics in the basins of southeastern Brazil, in *West Gondwana Pre-Cenozoic Correlations Across the South Atlantic Region*, edited by R. J. Pankhurst et al., *Geol. Soc. Spec. Publ.*, 294, 365–398.
- Moraes, M. A. S., W. B. Maciel, M. S. S. Braga, and A. R. Viana (2007), Bottom-current reworked Palaeocene-Eocene deep-water reservoirs of the Campos Basin, Brazil, in *Economic and Palaeoceanographic Significance of Contourite Deposits*, edited by A. R. Viana and M. Rebesco, *Geol. Soc. Spec. Publ.*, 276, 81–94.
- Moscardelli, L., and L. Wood (2008), New classification system for mass transport complexes in offshore Trinidad, *Basin Res.*, 20(1), 73–98, doi:10.1111/j.1365-2117.2007.00340.x.
- Moscardelli, L., L. Wood, and P. Mann (2006), Mass-transport complexes and associated processes in the offshore area of Trinidad and Venezuela, *AAPG Bull.*, 90(7), 1059–1088, doi:10.1306/02210605052.
- Nemec, W. (1990), Aspects of sediment movement on steep delta slopes, in *Coarse-Grained Deltas*, pp. 29–73, John Wiley, Hoboken, N. J.
- Odonne, F., P. Callot, E.-J. Debroas, T. Sempere, G. Hoareau, and A. Maillard (2011), Soft-sediment deformation from submarine sliding: Favourable conditions and triggering mechanisms in examples from the Eocene Sobrarbe delta (Ainsa, Spanish Pyrenees) and the mid-Cretaceous Ayabacas Formation (Andes of Peru), *Sediment. Geol.*, 235(3–4), 234–248, doi:10.1016/j.sedgeo.2010.09.013.
- Ojeda, H. A. O. (1982), Structural framework, stratigraphy, and evolution of Brazilian marginal basins, *AAPG Bull.*, 66(6), 732–749.
- Piper, D. J. W., C. Pirmez, P. L. Manley, D. Long, R. D. Flood, W. R. Normark, and W. Showers (1997), Mass transport deposits of the Amazon Fan, *Proc. Ocean Drill. Program Sci. Results*, 155, 109–146.
- Posamentier, H. W., and V. Kolla (2003), Seismic geomorphology and stratigraphy of depositional elements in deep-water settings, *J. Sediment. Res.*, 73(3), 367–388, doi:10.1306/111302730367.
- Sawyer, D. E., P. B. Flemings, B. Dugan, and J. T. Germaine (2009), Retrogressive failures recorded in mass transport deposits in the Ursa Basin, northern Gulf of Mexico, *J. Geophys. Res.*, 114, B10102, doi:10.1029/2008JB006159.
- Schultz-Ela, D. D., M. P. A. Jackson, and B. C. Vendeville (1993), Mechanics of active salt diapirism, *Tectonophysics*, 228(3–4), 275–312, doi:10.1016/0040-1951(93)90345-K.
- Seber, G. A. F., and A. J. Lee (2003), *Linear Regression Analysis*, 569 pp., John Wiley, Hoboken, N. J.
- Seni, S. J., and M. P. A. Jackson (1983), Evolution of salt structures, East Texas diapir province: Part I, Sedimentary record of halokinesis, *AAPG Bull.*, 67(8), 1219–1244.
- Shanmugam, G., R. B. Bloch, S. M. Mitchell, J. E. Damuth, G. W. J. Beamish, R. J. Hodgkinson, T. Straume, S. E. Syvertsen, and K. E. Shields (1996), Slump and debris-flow dominated basin-floor fans in the North Sea: An evaluation of conceptual sequence-stratigraphical models based on conventional core data, in *Sequence Stratigraphy in British Geology*, edited by S. P. Hesselbo and D. N. Parkinson, *Geol. Soc. Spec. Publ.*, 103, 145–176.
- Sheriff, R. E., and L. P. Geldart (1995), *Exploration Seismology*, 2nd ed., 628 pp., Cambridge Univ. Press, New York.
- Sobreira, J. F. F., and R. L. França (2005), A tectono-magmatic model for the Abrolhos Volcanic Complex region, *Bol. Geocienc. Petrobras*, 14(1), 143–147.
- Spence, G. H., and M. E. Tucker (1997), Genesis of limestone megabreccias and their significance in carbonate sequence stratigraphic models: A review, *Sediment. Geol.*, 112(3–4), 163–193, doi:10.1016/S0037-0738(97)00036-5.
- Tripsanas, E. K., W. R. Bryant, and B. A. Phaneuf (2004), Slope-instability processes caused by salt movements in a complex deep-water environment, Bryant Canyon area, northwest Gulf of Mexico, *AAPG Bull.*, 88(6), 801–823, doi:10.1306/01260403106.
- Tripsanas, E. K., D. J. W. Piper, K. A. Jenner, and W. R. Bryant (2008), Submarine mass-transport facies: New perspectives on flow processes from cores on the eastern North American margin, *Sedimentology*, 55(1), 97–136.
- Urgeles, R., J. Locat, and B. Dugan (2007), Recursive failure of the Gulf of Mexico continental slope: Timing and causes, in *Submarine Mass Movements and Their Consequences*, edited by V. Lykousis, D. Sakellariou, and J. Locat, pp. 209–219, Springer, New York, doi:10.1007/978-1-4020-6512-5\_22.
- Vendeville, B. (2002), A new interpretation of Trusheim's classic model of salt-diapir growth, *Trans. Gulf Coast Assoc. Geol. Soc.*, 52, 943–952.
- Welbon, A. I. F., P. J. Brockbank, D. Brunnsden, and T. S. Olsen (2007), Characterizing and producing from reservoirs in landslides: Challenges and opportunities, in *Structurally Complex Reservoirs*, edited by S. J. Jolley et al., *Geol. Soc. Spec. Publ.*, 292, 49–74.
- Zhang, L., X. Luo, Q. Liao, W. Yang, G. Vasseur, C. Yu, J. Su, S. Yuan, D. Xiao, and Z. Wang (2010), Quantitative evaluation of synsedimentary fault opening and sealing properties using hydrocarbon connection probability assessment, *AAPG Bull.*, 94(9), 1379–1399, doi:10.1306/12140909115.

T. Alves, J. Cartwright, and D. Gamboa, 3D Lab, School of Earth and Ocean Sciences, Cardiff University, Main Building, Park Place, CF10 3YE Cardiff, UK. (GamboaDA1@cf.ac.uk)